Computational homogenization of cellular materials

V.-D. Nguyen, L. Noels*

University of Liege (ULg),
Department of Aerospace and Mechanical Engineering,
Computational & Multiscale Mechanics of Materials
Chemin des Chevreuils 1, B-4000 Liège, Belgium

Abstract

In this work we propose to study the behavior of cellular materials using a second–order multi–scale computational homogenization approach. During the macroscopic loading, micro-buckling of thin components, such as cell walls or cell struts, can occur. Even if the behavior of the materials of which the micro–structure is made remains elliptic, the homogenized behavior can lose its ellipticity. In that case, a localization band is formed and propagates at the macro–scale. When the localization occurs, the assumption of local action in the standard approach, for which the stress state on a material point depends only on the strain state at that point, is no–longer suitable, which motivates the use of the second-order multi–scale computational homogenization scheme. At the macro–scale of this scheme, the discontinuous Galerkin method is chosen to solve the Mindlin strain gradient continuum. At the microscopic scale, the classical finite element resolutions of representative volume elements are considered. Since the meshes generated from cellular materials exhibit voids on the boundaries and are not conforming in general, the periodic boundary conditions are reformulated and are enforced by a polynomial interpolation method. With the presence of instability phenomena at both scales, the arc–length path following technique is adopted to solve both macroscopic and microscopic problems.

Keywords: Computational homogenization, Periodic condition, Honeycomb, Localization, Discontinuous Galerkin, FEM, Path following

1. Introduction

Nowadays, cellular materials are used in many engineering applications because of their attractive properties, e.g. light weight, high specific stiffness, good damping, high shock absorbability, etc [1]. Their mechanical properties depend not only on the intrinsic properties of the materials of which the cell walls and cell struts are made but also on the micro–morphology, i.e. the spatial distribution of cells (e.g. size, shape, etc). Because of the increase of material requirements for specific applications, for which the required mechanical properties can be achieved by manipulating the micro–structure, the relation between the structural behavior and the microscopic properties must be evaluated.

In experimental studies the cellular materials exhibit a complex mechanical behavior because of the presence of the size effects, as shown for example by Andrews et al. [2], and of the localization phenomena due to micro–buckling of thin components (cell walls, cell struts), as discussed for example by Papka et al. [3], Zhu et al. [4], Bart-Smith et al. [5], or Jang et al. [6], which may be enhanced by plastic deformation and reduces strongly the structural stiffness. In finite element analyzes, there are basically three different approaches used to study the behavior of cellular materials:

---

*Corresponding author; Phone: +32 4 366 4826; Fax: +32 4 366 9505
Email address: `L.Noels@ulg.ac.be` (L. Noels)

(i) the microscopic approach, (ii) the macroscopic approach, and (iii) the multi–scale computational approach. In the first approach, the detailed structure is considered by using the standard finite element formulation such as beam elements as proposed by Tekoglu et al. [7], Mangipudi et al. [8], Gibson and Ashby [1] and Chen et al. [9]. However, the use of direct simulations to model large problems by finite element analyzes can lead to an enormous number of unknowns. The solution of the resulting equations is still a challenge for actual modern computers. Therefore, this method is suitable for the problems with limited sizes. In the second one, the cellular structure is considered as a continuum medium and the phenomenological material model is applied, see for example the works by Forest et al. [10] and Hanssen et al. [11]. Although the efficiency is higher than for the first approach, this method is still limited by the fact that the material model and its parameters are difficult to be identified. Moreover the micro–structure evolution during the macroscopic loading cannot be observed. The last method, also–called FE[2], is a combination of the two first approaches in which two separate boundary value problems (BVPs) are defined at two separate scales, see Fig. 1. At the macroscopic scale, the macroscopic BVP is considered as a continuum medium and, at the microscopic scale, a microscopic BVP is associated to each macroscopic material point and contains all heterogeneities. Each microscopic BVP is defined on a representative volume element (RVE) and is associated with an appropriate microscopic boundary condition related to the macroscopic quantities, e.g macroscopic strains. The geometrical and material non–linearities at work on the micro–structure are explicitly modeled by using an arbitrary geometrically non–linear framework and arbitrary non–linear constitutive models. From the resolution of the microscopic BVPs, the macroscopic stress–strain relation is always available under the form of a homogenized constitutive law to be used in a macro–scale problem, see for example the developments by Yvonnet et al.[17], Laroussi et al. [18], Ohno et al. [19], and by Okumura et al. [20, 21], or under the form of a scale transition problem, see for example the developments by Sehlhorst et al. [12], Kouznetsova et al. [13, 14], Ebinger et al. [15], Onck et al. [16].
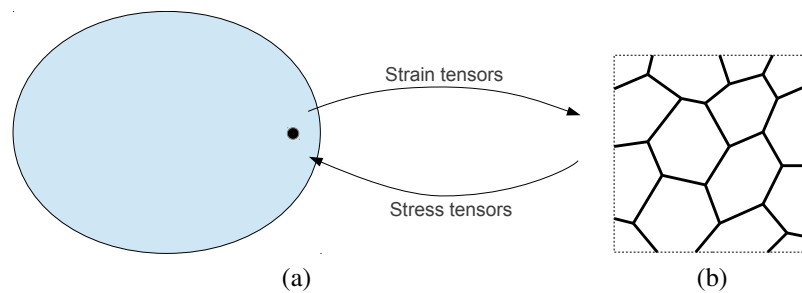

Figure 1. Multi–scale computational modeling of cellular materials: (a) macroscopic homogenized continuum medium, (b) micro–structure with cell walls and void parts. In the scale transition, the microscopic problem defines its boundary condition depending on the macroscopic strains and computes the macroscopic stresses and macroscopic tangents.

When considering FE[2] methods, the scale transition can be formulated as a first–order scheme by using the standard continuum theory at both macro– and micro–scales [12, 13] or as a second–order scheme with a generalized continuum theory applied at the macro–scale, e.g. a Cosserat continuum [15, 16] or a Mindlin strain gradient continuum [14]. Compared to the first–order schemes, the second–order ones can deal with size effects and some localization phenomena because of the accounting of the higher–order terms related to the higher–order strains (e.g. gradient of deformation gradient, etc). However, the second–order schemes cannot resolve the strong localization bands exhibiting deformations beyond a quadratic nature in the displacement field [22]. In case of a strong localization band, other approaches should be used, e.g. multi–scale enhanced schemes with a discontinuity enrichment at the macro–scale, see the work of Nguyen et al. [23], Massart et al. [24] and Coenen et al. [25]. In spite of their limitations, the second–order schemes are applicable for moderate localization phenomena in cellular materials. This work is thus restricted to the study of localization onsets and of moderate loadings for which the self–contact phenomena of cell walls have not yet happened.

In this work the presence of localization phenomena in cellular structures motivates the use of the second–order multi–scale computational homogenization scheme using a macroscopic Mindlin strain gradient continuum [14, 26, 27]. In this second–order scheme, both the deformation gradient and its gradient are used to define the microscopic boundary condition. The macroscopic stresses (first Piola–Kirchhoff and higher order ones) are calculated by using the generalized version of the Hill-Mandel homogenization principle. For cellular materials, the thickness of the

localization band is comparable to or slightly larger than the characteristic size of the micro–structure. As it will be shown in this paper, although we are clearly at the edge of the separation of scales, the second–order homogenization method remains accurate when the localization band present at the macroscopic scale is of a size larger than the RVE size. For periodic cellular materials it is the case as the microscopic BVP can be limited to a single cell study. In that case, the usual microscopic boundary conditions can still be used. Note however that to capture instability phenomena we introduce some different randomness in each micro–problem studied at each macroscopic Gauss point. As the instabilities are considered at both scales, the path following method [28, 29, 30, 31, 32, 33, 34, 35, 36] is used to solve both the macroscopic and the microscopic BVPs.

In order to solve the Mindlin strain gradient continuum in this second–order scheme, instead of using a specific finite element formulation as the mixed formulation [14, 26], an implementation based on a discontinuous Galerkin method is shown to be particularly efficient to constrain weakly the continuities of the displacement field and of its gradient [27]. This method can be easily integrated into conventional finite element codes and parallelized at the macroscopic scale by using face–based ghost elements [37, 38]. In that context the homogenization is viewed as a usual constitutive law from the macro-finite element, and this constitutive law solves another finite–element problem: the microscopic problem. In order to consider large problems, the multi–scale problem is not only parallelized at the macro–scale by face–based ghost elements but also by distributing the microscopic problems of a macro–partition between several processors.

At the microscopic scale, classical finite element resolutions of RVEs are considered. In a general problem, three classical boundary conditions, which are linear displacement boundary condition (Dirichlet condition), minimal kinematic boundary condition (Neumann condition) and periodic boundary condition can be used. Many numerical studies show that the periodic boundary condition provides a better estimation than other boundary condition types [39, 40, 41, 42]. For problems involving localization at the micro–scale, the boundary condition should be reformulated to account for this localization direction [43]. However, in this work, the localization bands at the macro–scale have a size larger than the size of the micro–scale problem and the classical microscopic boundary conditions can be used. The periodic boundary condition is chosen because of its efficiency. The implementation of the periodic boundary condition in case of conformal meshes is easy by constraining matching nodes. But meshes generated from the cellular materials are normally non–conformal because of their random spatial distribution. For these non–conformal meshes, some methods are available to enforce the periodic boundary condition in first–order schemes, such as the master/slave approach [44], the weak periodicity [41], the local implementation [45] and in a more general way as the interpolation polynomial interpolation [42]. As the two first methods cannot be used because of the dominant presence of voids on the boundary, see Fig. 1b, the polynomial interpolation method is adopted in this work and extended to the second–order FE[2] method.

The organization of the paper is as follows. In Section 2, the second–order multi–scale computational homogenization scheme is briefly recalled. The Section 3 presents the extension of the polynomial interpolation method for imposing the periodic boundary condition in the second–order scheme for micro–structures exhibiting many voids at the boundary. The path following method used for both the macroscopic and microscopic BVPs is presented in Section 4. We provide in Section 5 some numerical examples in which the ability of this approach to capture moderate localization bands is shown.

2. Second–order multi–scale computational homogenization approach

In this section, the second–order multi–scale computational homogenization approach (see Fig. 1) based on the discontinuous Galerkin (DG) formulation [27] is briefly recalled. Within this scheme, the macroscopic Mindlin strain gradient continuum is solved by using the DG method while the microscopic problem is solved by using the classical finite element formulation.

2.1. Macroscopic discontinuous Galerkin formulation

When using the total Lagrange approach, the first Piola–Kirchhoff stress $\bar{\mathbf{P}}$ and the higher–order stress $\bar{\mathbf{Q}}$, which are energetically conjugate with the deformation gradient $\bar{\mathbf{F}} = \mathbf{I} + \bar{\mathbf{u}} \otimes \boldsymbol{\nabla}_0$ and its gradient $\bar{\mathbf{G}} = \bar{\mathbf{F}} \otimes \boldsymbol{\nabla}_0 = \bar{\mathbf{u}} \otimes \boldsymbol{\nabla}_0 \otimes \boldsymbol{\nabla}_0$ respectively, are used to formulate the continuum theory. The higher–order stress and the gradient of deformation

gradient are third order tensors and satisfy the symmetrical properties $\bar{Q}_{ijk} = \bar{Q}_{ikj}$ and $\bar{G}_{ijk} = \bar{G}_{ikj}$. The strong form of the Mindlin strain gradient continuum [13, 46] is given in the body B_0 by

$$\bar{\mathbf{P}}\left(\bar{\mathbf{X}}\right) \cdot \boldsymbol{\nabla}_0 - \bar{\mathbf{Q}}\left(\bar{\mathbf{X}}\right) : \left(\boldsymbol{\nabla}_0 \otimes \boldsymbol{\nabla}_0\right) = \mathbf{0} \quad \forall \bar{\mathbf{X}} \in B_0\,. \tag{1}$$

Besides the classical boundary conditions related to the displacement $\bar{\mathbf{u}}$ on the Dirichlet boundary part and to the traction per reference unit surface $\bar{\mathbf{T}}$ on the Neumann boundary part, the high–order boundary conditions of normal gradient of displacement $\mathrm{D}\bar{\mathbf{u}}$ and of the double traction per reference unit surface $\bar{\mathbf{R}}$ are added to complete the formulation statement. These boundary conditions are

$$\begin{cases} \bar{\mathbf{u}} = \bar{\mathbf{u}}^0 & \forall \bar{\mathbf{X}} \in \partial_D B_0\,, \\ \bar{\mathbf{T}} = \bar{\mu}\bar{\mathbf{T}}^0 & \forall \bar{\mathbf{X}} \in \partial_N B_0\,, \\ \mathrm{D}\bar{\mathbf{u}} = \mathrm{D}\bar{\mathbf{u}}^0 & \forall \bar{\mathbf{X}} \in \partial_T B_0\,, \\ \bar{\mathbf{R}} = \bar{\mu}\bar{\mathbf{R}}^0 & \forall \bar{\mathbf{X}} \in \partial_M B_0\,, \end{cases} \tag{2}$$

where the traction per reference unit surface $\bar{\mathbf{T}}$ is given by

$$\bar{\mathbf{T}} = \left(\bar{\mathbf{P}} - \bar{\mathbf{Q}} \cdot \boldsymbol{\nabla}_0\right) \cdot \bar{\mathbf{N}} + \left(\mathbf{Q} \cdot \bar{\mathbf{N}}\right) \cdot \left(\bar{\mathbf{N}} \overset{s}{\boldsymbol{\nabla}_0} \cdot \bar{\mathbf{N}} - \overset{s}{\boldsymbol{\nabla}_0}\right)\,, \tag{3}$$

where the double stress $\bar{\mathbf{R}}$ is given by

$$\bar{\mathbf{R}} = \bar{\mathbf{Q}} : \left(\bar{\mathbf{N}} \otimes \bar{\mathbf{N}}\right)\,, \tag{4}$$

where the normal gradient and surface gradient operators are respectively defined by

$$\mathrm{D} = \bar{\mathbf{N}} \cdot \boldsymbol{\nabla}_0\,, \tag{5}$$

$$\overset{s}{\boldsymbol{\nabla}_0} = \left(\mathbf{I} - \bar{\mathbf{N}} \otimes \bar{\mathbf{N}}\right) \cdot \boldsymbol{\nabla}_0\,, \tag{6}$$

where $\bar{\mathbf{N}}$ is the outward normal in the reference configuration, and where $\bar{\mu}$ is the load parameter that gives the load intensity with a view to the introduction of the path following method. The strain gradient problem (1) with its boundary conditions (2) is completed by the constitutive law specifying the stress–strain relationships at time t:

$$\begin{aligned} \bar{\mathbf{P}}(t) &= \mathfrak{P}\left\{\bar{\mathbf{F}}(\tau), \bar{\mathbf{G}}(\tau), \tau \in [0\,,t]\right\} \text{ and} \\ \bar{\mathbf{Q}}(t) &= \mathfrak{Q}\left\{\bar{\mathbf{F}}(\tau), \bar{\mathbf{G}}(\tau), \tau \in [0\,,t]\right\}\,. \end{aligned} \tag{7}$$

In the multiscale framework, these relationships are obtained from the resolutions of the micro–scale problems as explained in Section 2.2.

The macroscopic problem defined by the Eqs. (1, 2, 7) is solved by recourse to the DG method as proposed by Nguyen et al. [27]. In this method, the body B_0 is discretized into finite elements Ω_0^e, see Fig. 2. The C^1 continuity of the displacement field across the element boundaries is weakly enforced while the C^0 continuity can be either weakly imposed using the DG method or strongly constrained using the conventional C^0 displacement–based finite element formulation. Thus, two formulations can be used: (i) the full DG (FDG) formulation, which constrains weakly the C^0 and C^1 continuities and (ii) the enriched DG (EDG) formulation for which some higher–order terms are added into the conventional C^0 finite element framework. Because the FDG formulation allows the jump discontinuities of the displacement field and of its gradient, the definitions of its displacement manifold and of its constrained counterpart are given by

$$\mathbf{U}^k = \left\{\bar{\mathbf{u}} \in \mathbf{L}^2\left(B_0\right) \quad | \quad \bar{\mathbf{u}}|_{\Omega_0^e} \in \mathbb{P}^k \quad \forall \Omega_e^0 \in B_0\right\}\,, \tag{8}$$

$$\mathbf{U}_c^k = \left\{\delta\bar{\mathbf{u}} \in \mathbf{U}^k \quad | \quad \delta\bar{\mathbf{u}}|_{\partial_D B_0} = \mathbf{0}\right\}\,, \tag{9}$$
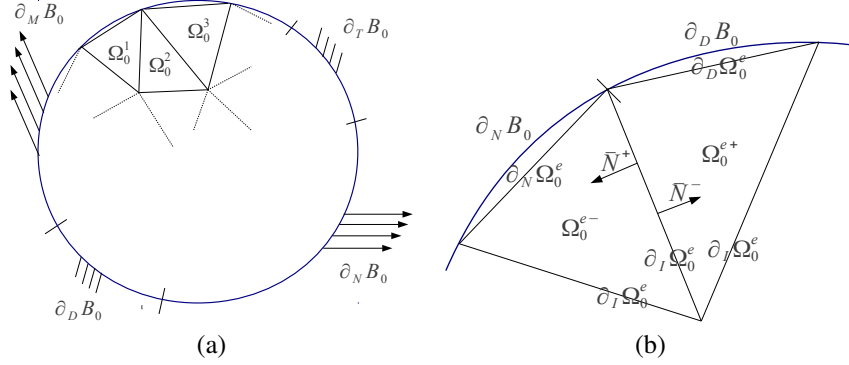
Figure 2. Finite element discretization of the reference body B_0: (a) finite element mesh and (b) details of two adjacent elements. The element boundary, the internal boundary and the outward normals between two elements are represented.

where $\mathbb{P}^k$ is the space of polynomial functions of order up to k with support Ω_0^e. The functional spaces of the EDG formulation are easily deduced by defining

$$\mathbf{U}^k \quad = \left\{ \bar{\mathbf{u}} \in \mathbf{H}^1\left(B_0\right) \quad | \quad \bar{\mathbf{u}}|_{\Omega_0^e} \in \mathbb{P}^k \quad \forall \Omega_e^0 \in B_0 \right\}, \tag{10}$$

$$\mathbf{U}_c^k \quad = \left\{ \delta\bar{\mathbf{u}} \in \mathbf{U}^k \quad | \quad \delta\bar{\mathbf{u}}|_{\partial_D B_0} = \mathbf{0} \right\}, \tag{11}$$

in which the discontinuities in $\bar{\mathbf{u}}$ and $\delta\bar{\mathbf{u}}$ simply vanish from the formulation. Considering a DG formulation allows the strain–gradient continuum to be solved using traditional finite elements. Usual continuous shape functions are considered in the EDG formulation and the number of degrees of freedom in this case is the same as for conventional C^0 finite elements. On the contrary, the FDG method suffers from an explosion in the number of degrees of freedom at the macroscopic scale as the shape functions are now discontinuous. However, in the computational multiscale framework the computational resources are mainly due to the resolutions of the microscopic problems, so that the FDG method remains attractive in the case of parallel implementations as it allows using face–based ghost elements [37, 38].

The details of the mathematical developments to establish the DG formulation are presented in [27] and are summarized as finding $\bar{\mathbf{u}} \in \mathbf{U}^k$ such that

$$\mathrm{a}\left(\bar{\mathbf{u}}, \delta\bar{\mathbf{u}}\right) = \mathrm{b}\left(\delta\bar{\mathbf{u}}\right) \qquad \forall \delta\bar{\mathbf{u}} \in \mathbf{U}_c^k, \tag{12}$$

where the linear term $\mathrm{b}\left(\delta\bar{\mathbf{u}}\right)$ is given by

$$\mathrm{b}\left(\delta\bar{\mathbf{u}}\right) = \bar{\mu}\left(\int_{\partial_N B_0} \bar{\mathbf{T}}^0 \cdot \delta\bar{\mathbf{u}}\, d\partial B + \int_{\partial_M B_0} \bar{\mathbf{R}}^0 \cdot \mathrm{D}\delta\bar{\mathbf{u}}\, d\partial B\right), \tag{13}$$

and where the term $\mathrm{a}\left(\bar{\mathbf{u}}, \delta\bar{\mathbf{u}}\right)$ is given by

$$\mathrm{a}\left(\bar{\mathbf{u}}, \delta\bar{\mathbf{u}}\right) = \mathrm{a}^{\mathrm{bulk}}\left(\bar{\mathbf{u}}, \delta\bar{\mathbf{u}}\right) + \mathrm{a}^{\mathrm{PI}}\left(\bar{\mathbf{u}}, \delta\bar{\mathbf{u}}\right) + \mathrm{a}^{\mathrm{QI}}\left(\bar{\mathbf{u}}, \delta\bar{\mathbf{u}}\right), \tag{14}$$

with the bulk term

$$\mathrm{a}^{\mathrm{bulk}}\left(\bar{\mathbf{u}}, \delta\bar{\mathbf{u}}\right) = \int_{B_0} \left[\bar{\mathbf{P}}\left(\bar{\mathbf{u}}\right) : \bar{\mathbf{F}}\left(\delta\bar{\mathbf{u}}\right) + \bar{\mathbf{Q}}\left(\bar{\mathbf{u}}\right) \vdots \bar{\mathbf{G}}\left(\delta\bar{\mathbf{u}}\right)\right] dB, \tag{15}$$

with the first–order interface terms

$$a^{PI}(\bar{\mathbf{u}}, \delta\bar{\mathbf{u}}) = \int_{\partial_I B_0} \left[[\![\delta\bar{\mathbf{u}}]\!] \cdot \left\langle \tilde{\bar{\mathbf{P}}}(\bar{\mathbf{u}}) \right\rangle \cdot \bar{\mathbf{N}}^- + [\![\bar{\mathbf{u}}]\!] \cdot \left\langle \tilde{\bar{\mathbf{P}}}(\delta\bar{\mathbf{u}}) \right\rangle \cdot \bar{\mathbf{N}}^- \right.$$
$$\left. + [\![\bar{\mathbf{u}}]\!] \otimes \bar{\mathbf{N}}^- : \left\langle \frac{\beta_P}{h_s} \mathbf{C}^0 \right\rangle : [\![\delta\bar{\mathbf{u}}]\!] \otimes \bar{\mathbf{N}}^- \right] d\partial B, \tag{16}$$

and with the second–order interface terms

$$a^{QI}(\bar{\mathbf{u}}, \delta\bar{\mathbf{u}}) = \int_{\partial_I B_0} \left[[\![\delta\bar{\mathbf{u}} \otimes \mathbf{\nabla}_0]\!] : \left\langle \bar{\mathbf{Q}}(\bar{\mathbf{u}}) \right\rangle \cdot \bar{\mathbf{N}}^- + [\![\bar{\mathbf{u}} \otimes \mathbf{\nabla}_0]\!] : \left\langle \bar{\mathbf{Q}}(\delta\bar{\mathbf{u}}) \right\rangle \cdot \bar{\mathbf{N}}^- \right.$$
$$\left. + [\![\bar{\mathbf{u}} \otimes \mathbf{\nabla}_0]\!] \otimes \bar{\mathbf{N}}^- \vdots \left\langle \frac{\beta_Q}{h_s} \mathbf{J}^0 \right\rangle \vdots [\![\delta\bar{\mathbf{u}} \otimes \mathbf{\nabla}_0]\!] \otimes \bar{\mathbf{N}}^- \right] d\partial B. \tag{17}$$

In these interface terms, $\tilde{\bar{\mathbf{P}}} = \bar{\mathbf{P}} - \bar{\mathbf{Q}} \cdot \mathbf{\nabla}_0$, $\mathbf{C}^0 = \frac{\partial \bar{\mathbf{P}}}{\partial \bar{\mathbf{F}}}$ is the tangent operator of the constitutive law $\bar{\mathbf{P}}$ in terms of the deformation gradient $\bar{\mathbf{F}}$, $\mathbf{J}^0 = \frac{\partial \bar{\mathbf{Q}}}{\partial \bar{\mathbf{G}}}$ is the higher–order tangent operator of the constitutive law $\bar{\mathbf{Q}}$ in terms of the higher–order gradient $\bar{\mathbf{G}}$, and β_P and β_Q are the stability parameters. As the sole purpose of the quadratic terms is to ensure the stability of the method, $\mathbf{C}^0$ and $\mathbf{J}^0$ can be chosen constant during the simulations and are evaluated at the zero–strain state corresponding to $\bar{\mathbf{F}} = \mathbf{I}$ and $\bar{\mathbf{G}} = \mathbf{0}$, which explains the superscript 0. Using these tensors has two advantages. On the one hand, it avoids evaluating their derivatives during the Newton–Raphson iterations, and on the other hand, it prevents the stability terms to vanish in case of material softening [27].

The two interface terms (16) and (17) are typical from a DG formulation and they ensure the consistency of the method, the compatibility of the field (derivatives) and the stability of the methodology by the parameters β_P and β_Q. These interface terms are computed on the interfaces between two finite elements, see Fig. 2, and require the evaluation of the jump and mean values defined by

$$[\![\bullet]\!] = \bullet^+ - \bullet^- \text{ and} \tag{18}$$

$$\langle \bullet \rangle = \frac{1}{2}(\bullet^+ + \bullet^-), \tag{19}$$

where the bullets represent a generic field with

$$\bullet^+ = \lim_{\varepsilon \to 0^+} \bullet\left(\bar{\mathbf{X}} + \varepsilon\bar{\mathbf{N}}^-\right) \text{ and } \bullet^- = \lim_{\varepsilon \to 0^+} \bullet\left(\bar{\mathbf{X}} - \varepsilon\bar{\mathbf{N}}^-\right). \tag{20}$$

In case of the EDG formulation, the first–order term $a^{PI}(\bar{\mathbf{u}}, \delta\bar{\mathbf{u}})$ vanishes and only $a^{QI}(\bar{\mathbf{u}}, \delta\bar{\mathbf{u}})$ remains.

When considering a finite element approximation, the weak form (12) is equivalent to the non–linear equation

$$\bar{\mathbf{f}}_{\text{int}}(\bar{\mathbf{u}}) - \bar{\mu}\bar{\mathbf{q}} = \mathbf{0}, \tag{21}$$

where $\bar{\mathbf{f}}_{\text{int}}(\bar{\mathbf{u}})$ is the internal force computed from the bulk and surface integrals and where

$$\bar{\mathbf{q}} = \int_{\partial_N B_0} \bar{\mathbf{T}}^0 \cdot \delta\bar{\mathbf{u}} \, d\partial B + \int_{\partial_M B_0} \bar{\mathbf{R}}^0 \cdot D\delta\bar{\mathbf{u}} \, d\partial B. \tag{22}$$

2.2. Microscopic classical continuum

In the second–order homogenization scheme, the microscopic problem is formulated in the classical continuum. By using the total Lagrange approach, the problem is formulated in terms of the first Piola–Kirchhoff stress $\mathbf{P}$ and of the deformation gradient $\mathbf{F} = \mathbf{I} + \mathbf{u} \otimes \mathbf{\nabla}_0$. The BVP is defined on a representative volume element (RVE) V_0 of boundary ∂V_0. In the absence of the body forces, the strong form is given by

$$\mathbf{P}(\mathbf{X}) \otimes \mathbf{\nabla}_0 = \mathbf{0} \quad \forall \mathbf{X} \in V_0. \tag{23}$$

$$\mathbf{x} = \bar{\mathbf{F}} \cdot \mathbf{X} + \tfrac{1}{2}\bar{\mathbf{G}} : (\mathbf{X} \otimes \mathbf{X}) + \mathbf{w}$$
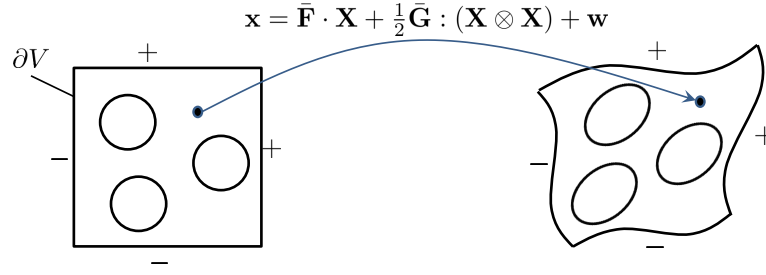
Figure 3. Deformation of a square–shaped representative volume element. The deformation configuration is driven by the macroscopic deformation gradient $\bar{\mathbf{F}}$ and by its gradient $\bar{\mathbf{G}}$. The non–linear mapping $\mathbf{x}$ is composed of the homogeneous part $\bar{\mathbf{F}} \cdot \mathbf{X} + \frac{1}{2}\bar{\mathbf{G}} : (\mathbf{X} \otimes \mathbf{X})$ and of the fluctuation part $\mathbf{w}$. The positive and negative parts of the RVE boundary are depicted.

In order to achieve the scale transition, the boundary condition results from the macroscopic variables, and the microscopic fluctuation of displacement field $\mathbf{w}$ on the RVE is defined as

$$\mathbf{w} = \mathbf{u} - \left(\bar{\mathbf{F}} - \mathbf{I}\right) \cdot \mathbf{X} + \frac{1}{2}\bar{\mathbf{G}} : (\mathbf{X} \otimes \mathbf{X}) , \tag{24}$$

where $\mathbf{u}$ is the displacement field on the RVE and where $\bar{\mathbf{F}}$ and $\bar{\mathbf{G}}$ are respectively the macroscopic deformation gradient and its gradient obtained from the macroscopic problem. The deformation of a square–shaped RVE sample under the effect of the macroscopic strains with the fluctuation $\mathbf{w}$ is shown in Fig. 3. The kinematic constraints

$$\frac{1}{V_0} \int_{V_0} \mathbf{F} \, dV = \bar{\mathbf{F}} \tag{25}$$

is *a priori* satisfied by the second–order periodic boundary condition [14, 26, 27], which leads to the following kinematic constraints of the fluctuation field on the RVE boundary

$$\mathbf{w}(\mathbf{X}^+) = \mathbf{w}(\mathbf{X}^-) \qquad \forall \mathbf{X}^- \in \partial V_0^- \text{ and matching } \mathbf{X}^+ \in \partial V_0^+ , \text{ and} \tag{26}$$

$$\int_{S_i} \mathbf{w}(\mathbf{X}) \, d\partial V = \mathbf{0} \quad \forall S_i \subset \partial V_0^- , \tag{27}$$

where ∂V_0^- and ∂V_0^+ are respectively the negative and positive parts of the boundary ∂V_0 and where S_i is one surface on the negative part ∂V_0^-, see Fig. 3.

The continuum problem (23) with its boundary conditions (24, 26, 27) is completed by the constitutive law specifying the stress–strain relationship at time t:

$$\mathbf{P}(t) = \mathfrak{F}\{\mathbf{F}(\tau), \tau \in [0, t]\} . \tag{28}$$

This relationship is detailed in Appendix A in the case of elasto–plastic materials.

Using a finite element analysis to solve (23) and using the Lagrange multipliers λ to take into account the kinematic constraints resulting from Eqs. (24, 26, 27), see [47, 27], lead to the microscopic non–linear equations rewritten in the matrix form as

$$\begin{cases} \mathbf{f}_{\text{int}}(\mathbf{w}) = \mathbf{C}^T \lambda , \\ \mathbf{C}\mathbf{w} = \mathbf{0} , \end{cases} \tag{29}$$

where $\mathbf{C}$ is the constraints matrix. This matrix is detailed in the next section in case of cellular materials.

2.3. Scale transition

For the scale transition, the generalized version of Hill–Mandel homogenization principle [13] is satisfied as

$$\bar{\mathbf{P}} : \delta\bar{\mathbf{F}} + \bar{\mathbf{Q}} \vdots \delta\bar{\mathbf{G}} = \frac{1}{V_0} \int_{V_0} \mathbf{P} : \delta\mathbf{F}\, dV \,, \tag{30}$$

and the macroscopic stresses are given by

$$\bar{\mathbf{P}} = \frac{1}{V_0} \int_{V_0} \mathbf{P}\, dV \text{ and} \tag{31}$$

$$\bar{\mathbf{Q}} = \frac{1}{2V_0} \int_{V_0} \mathbf{P} \otimes \mathbf{X} + (\mathbf{P} \otimes \mathbf{X})^{RC}\, dV \,, \tag{32}$$

where $A^{RC}_{ijk} = A_{ikj}$ is the right transpose of any third order tensor $\mathbf{A}$. From the homogenized stresses, the first–order and second–order tangents are respectively defined by

$$\bar{\mathbf{L}} = \frac{\partial\bar{\mathbf{P}}}{\partial\bar{\mathbf{F}}} \text{ and } \bar{\mathbf{J}} = \frac{\partial\bar{\mathbf{Q}}}{\partial\bar{\mathbf{G}}} \,. \tag{33}$$

and the cross tangents are defined by

$$\bar{\mathbf{L}}_J = \frac{\partial\bar{\mathbf{P}}}{\partial\bar{\mathbf{G}}} \text{ and } \bar{\mathbf{J}}_L = \frac{\partial\bar{\mathbf{Q}}}{\partial\bar{\mathbf{F}}} \,. \tag{34}$$

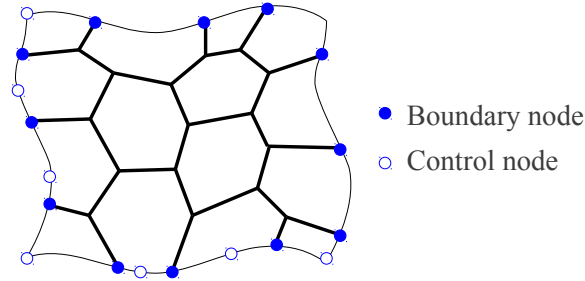## 3. Second–order periodic boundary condition with the polynomial interpolation method

Figure 4. The polynomial interpolation method to enforce the periodic boundary condition on a representative volume element with the presence of void parts on the boundary.

The enforcement of the periodic boundary condition for conforming meshes can easily be done by directly constraining the matching nodes. For cellular materials, since the obtained meshes are normally non–conforming (in this paper this is due to the perturbations introduced), the matching nodes method cannot be applied. Moreover, if the RVE boundary possesses a dominant void part, the constraint (27) can be divided into the solid integral term computed on S_i^{solid} and the void integral term computed on S_i^{void} such as

$$\int_{S_i} \mathbf{w}(\mathbf{X})\, d\partial V = \int_{S_i^{\text{solid}}} \mathbf{w}(\mathbf{X})\, d\partial V + \int_{S_i^{\text{void}}} \mathbf{w}(\mathbf{X})\, d\partial V = \mathbf{0} \,. \tag{35}$$

Because there is no material on S_i^{void}, the void integral term is non-determined and the constraint (27) cannot be enforced. This motivates the use of other methods for a general mesh setting.

Some methods for non–conformal meshes are available in the literature as the weak periodicity approach [41], the master/slave approach [44], the local implementation approach [45] and the polynomial interpolation approach [42]

for examples. Among these methods, only the polynomial interpolation method [42] is suitable for enforcing both the periodicity on non–conformal meshes and the constraint (27) with the presence of void parts on the RVE boundary.

The basic idea of the polynomial interpolation method is to guarantee the periodic boundary condition by interpolating the perturbation field on the negative and positive parts of the RVE boundary with one interpolant function whose form is defined. This interpolation requires a set of control nodes which can be created or chosen from existing ones. An example of distribution of control nodes and boundary nodes on the RVE boundary is shown in Fig. 4 in which the set of control nodes is added on the negative part. The periodic boundary condition with constraints (26, 27) are respectively rewritten in the interpolation form, as

$$\mathbf{w}^{-}(\mathbf{X}) = \sum_{k} \mathbb{N}^{k}(\mathbf{X})\, \mathbf{w}^{k} + \sum_{k} \mathbb{M}^{k}(\mathbf{X})\, \boldsymbol{\theta}^{k}\,, \tag{36}$$

$$\mathbf{w}^{+}(\mathbf{X}) = \sum_{k} \mathbb{N}^{k}(\mathbf{X})\, \mathbf{w}^{k} + \sum_{k} \mathbb{M}^{k}(\mathbf{X})\, \boldsymbol{\theta}^{k} \text{ and} \tag{37}$$

$$\int_{S \subset \partial V^{-}} \left(\sum_{k} \mathbb{N}^{k}(\mathbf{X})\, \mathbf{w}^{k} + \sum_{k} \mathbb{M}^{k}(\mathbf{X})\, \boldsymbol{\theta}^{k} \right) d\partial V = \mathbf{0}\,, \tag{38}$$

where $\mathbf{w}^{k}$ and $\boldsymbol{\theta}^{k}$ are respectively the fluctuation and additional unknowns at the control node k. The choice of $\mathbf{w}^{k}$ and $\boldsymbol{\theta}^{k}$ depends on the nature of the interpolant functions $\mathbb{N}(\mathbf{X})$ and $\mathbb{M}(\mathbf{X})$. For example, if the Lagrange formulation is used, only $\mathbf{w}^{k}$ is used while if the cubic spline formulation is used $\boldsymbol{\theta}^{k}$, known as the tangent at segment extremities, is added, see [42]. Note that the last equation (38), which corresponds to the equation (27), is equivalent to fix the rigid body modes.

Using Eq. (24), the periodic boundary condition of the second–order scheme is rewritten in terms of the displacement unknowns, yielding

$$\mathbf{u}^{-}(\mathbf{X}) - \sum_{k} \mathbb{N}^{k}(\mathbf{X})\, \mathbf{u}^{k} - \sum_{k} \mathbb{M}^{k}(\mathbf{X})\, \boldsymbol{\theta}^{k} = \bar{\mathbf{F}} \cdot \left[\mathbf{X} - \sum_{k} \mathbb{N}^{k}(\mathbf{X})\, \mathbf{X}^{k} \right]$$
$$+ \frac{1}{2}\bar{\mathbf{G}} : \left[\mathbf{X} \otimes \mathbf{X} - \sum_{k} \mathbb{N}^{k}(\mathbf{X})\, \mathbf{X}^{k} \otimes \mathbf{X}^{k} \right], \tag{39}$$

$$\mathbf{u}^{+}(\mathbf{X}) - \sum_{k} \mathbb{N}^{k}(\mathbf{X})\, \mathbf{u}^{k} - \sum_{k} \mathbb{M}^{k}(\mathbf{X})\, \boldsymbol{\theta}^{k} = \bar{\mathbf{F}} \cdot \left[\mathbf{X} - \sum_{k} \mathbb{N}^{k}(\mathbf{X})\, \mathbf{X}^{k} \right]$$
$$+ \frac{1}{2}\bar{\mathbf{G}} : \left[\mathbf{X} \otimes \mathbf{X} - \sum_{k} \mathbb{N}^{k}(\mathbf{X})\, \mathbf{X}^{k} \otimes \mathbf{X}^{k} \right] \text{ and} \tag{40}$$

$$\int_{S \subset \partial V^{-}} \left(\sum_{k} \mathbb{N}_{k}(\mathbf{X})\, \mathbf{u}^{k} + \sum_{k} \mathbb{M}^{k}(\mathbf{X})\, \boldsymbol{\theta}^{k} \right) d\partial V = \bar{\mathbf{F}} \cdot \left[\int_{S \in \partial V^{-}} \sum_{k} \mathbb{N}_{k}(\mathbf{X})\, \mathbf{X}^{k}\, d\partial V \right]$$
$$+ \frac{1}{2}\bar{\mathbf{G}} \cdot \left[\int_{S \in \partial V^{-}} \sum_{k} \mathbb{N}_{k}(\mathbf{X})\, \mathbf{X}^{k} \otimes \mathbf{X}^{k}\, d\partial V \right]. \tag{41}$$

By regrouping all the degrees of freedom of the boundary and control nodes in a unique vector $\tilde{\mathbf{u}}_{b}$, the interpolation form of the periodic boundary condition in the second–order scheme reads in the general matrix form

$$\tilde{\mathbf{C}}\tilde{\mathbf{u}}_{b} - \mathbf{g}\left(\bar{\mathbf{F}}, \bar{\mathbf{G}}\right) = \mathbf{0}\,, \tag{42}$$

where $\tilde{\mathbf{C}}$ and $\mathbf{g}$ are respectively the constraint coefficients matrix and the loading part which depends only on the macroscopic strains for a specific RVE.

With a view toward the use of a path following method, the macroscopic strains are parametrized by a scalar

variable μ with respect to the macroscopic strains such that

$$\bar{\mathbf{F}}(\mu) = \bar{\mathbf{F}}_0 + \mu \left(\bar{\mathbf{F}}_1 - \bar{\mathbf{F}}_0 \right) = \bar{\mathbf{F}}_0 + \mu \Delta \bar{\mathbf{F}} \text{ and} \tag{43}$$

$$\bar{\mathbf{G}}(\mu) = \bar{\mathbf{G}}_0 + \mu \left(\bar{\mathbf{G}}_1 - \bar{\mathbf{G}}_0 \right) = \bar{\mathbf{G}}_0 + \mu \Delta \bar{\mathbf{G}} , \tag{44}$$

where $\mu \in [0\ 1]$ and where the subscripts 0 and 1 denote the macroscopic previous and current strains respectively.

Using this parametrization, the right hand side $\mathbf{g}$ of Eq. (42) becomes

$$\mathbf{g}(\mu) = \mathbf{g} \left(\bar{\mathbf{F}}_0, \bar{\mathbf{G}}_0 \right) + \mathbf{q} \left(\Delta \bar{\mathbf{F}}, \Delta \bar{\mathbf{G}} \right) \mu = \mathbf{g}_0 + \mathbf{q}\mu \quad \text{with } \mathbf{q} = \frac{\partial \mathbf{g}}{\partial \mu} . \tag{45}$$

Equation (42) is thus rewritten in terms of the displacements vector $\mathbf{u}$ of the microscopic problem as

$$\mathbf{C}\mathbf{u} - \mathbf{g}_0 - \mathbf{q}\mu = \mathbf{0} , \tag{46}$$

where $\mathbf{C}$ is the constraint matrix built from the boundary constraint matrix $\tilde{\mathbf{C}}$. Finally the non–linear system of equations (29) with linear constraints is rewritten in terms of the structural displacement vector as

$$\begin{cases} \mathbf{f}_{\text{int}}(\mathbf{u}) - \mathbf{C}^T \lambda = \mathbf{0} , \\ \mathbf{C}\mathbf{u} - \mathbf{g}_0 - \mathbf{q}\mu = \mathbf{0} , \\ \mu = 1 \end{cases} \tag{47}$$

where the last equation $\mu = 1$ implies the final equilibrium state corresponding to the applied macroscopic strains. The non–linear system (47) is resolved by using the constraint projection strategy [26, 27] combined with the path following method with arc–length increment control as detailed in section 4.

4. Path following strategy

The non–linear response of a structural analysis can be characterized by the presence of critical points and unstable equilibrium paths. Because of these structural instabilities, the convergence of the conventional Newton–Raphson strategy with a constant load during each loading step usually fails. As the path following method combined with the arc–length increment constraint is commonly used to pass these critical points and to capture softening responses, see *e.g.* [28, 29, 30, 31, 32] for elastic problems and *e.g.* [33, 34, 35, 36] for elasto–plastic problems, this method is adopted in this work.

4.1. Solution of the macroscopic BVP

The macroscopic state vector is defined as $[\bar{\mathbf{u}}^T \ \bar{\mu}]^T$. Because the previous state $[\bar{\mathbf{u}}_n^T \ \bar{\mu}_n]^T$ is known, the current state $[\bar{\mathbf{u}}_{n+1}^T \ \bar{\mu}_{n+1}]^T$ is determined by finding a displacement increment $\Delta \bar{\mathbf{u}}_{n+1}$ and a load parameter increment $\Delta \bar{\mu}_{n+1}$ such that

$$\bar{\mathbf{u}}_{n+1} = \bar{\mathbf{u}}_n + \Delta \bar{\mathbf{u}}_{n+1} \text{ and} \tag{48}$$

$$\bar{\mu}_{n+1} = \bar{\mu}_n + \Delta \bar{\mu}_{n+1} , \tag{49}$$

for each arc–length increment ΔL which can be approximated by

$$\Delta L = \sqrt{\frac{\Delta \bar{\mathbf{u}}_{n+1}^T \Delta \bar{\mathbf{u}}_{n+1}}{\Psi^2} + \Delta \bar{\mu}_{n+1}^2} , \tag{50}$$

where Ψ is a constant parameter used to yield a dimensionless equation as the dimensions of $\Delta \bar{\mathbf{u}}_{n+1}$ and $\Delta \bar{\mu}_{n+1}$ are different. The value of Ψ is set at the computation beginning by an arbitrary value which has same magnitude as the

displacement solution. The arc–length increment (50) leads to the quadratic constraint

$$\bar{h}(\Delta\bar{\mathbf{u}}_{n+1}, \Delta\bar{\mu}_{n+1}) = \frac{\Delta\bar{\mathbf{u}}_{n+1}^T \Delta\bar{\mathbf{u}}_{n+1}}{\Psi^2} + \Delta\bar{\mu}_{n+1}^2 - \Delta L^2 = 0\,. \tag{51}$$

Thus the system of the non–linear equations (21) is completed by the arc–length constraint (51). From the definition of the macroscopic residual force

$$\bar{\mathbf{r}} = \bar{\mathbf{f}}_{\text{int}} - \bar{\mathbf{q}}\bar{\mu}, \tag{52}$$

the non–linear system

$$\begin{cases} \bar{\mathbf{r}}(\Delta\bar{\mathbf{u}}_{n+1}, \Delta\bar{\mu}_{n+1}, \bar{\alpha}_{n+1}^i; \bar{\alpha}_n^i) = \mathbf{0}\,, \\ \bar{h}(\Delta\bar{\mathbf{u}}_{n+1}, \Delta\bar{\mu}_{n+1}) = 0\,, \end{cases} \tag{53}$$

must be iteratively solved to find the displacement and the load parameter increments. In Eq. (53), $\bar{\alpha}_{n+1}^i$ and $\bar{\alpha}_n^i$ are the internal variables of the macroscopic problem, *i.e.* the complete state definition of the associated microscopic problems, at time steps $n + 1$ and n respectively. The values $\bar{\alpha}_n^i$ are known from the converged step n.

The resolution of the system of equations (53) follows the predictor–corrector scheme with an arc–length increment $\Delta L = L_{n+1} - L_n$ for the arc–length interval $[L_n \; L_{n+1}]$. The predictor and corrector steps are summarized as follows. Note that the symbols n and k denote respectively the step and the iteration indexes.

1. Macroscopic predictor step: $k = 0$

   - The macroscopic force residual is first linearized around the converged solution at the arc–length increment as

     $$\bar{\mathbf{r}}(\Delta\bar{\mathbf{u}}_{n+1}, \Delta\bar{\mu}_{n+1}, \bar{\alpha}_{n+1}^i; \bar{\alpha}_n^i) = \bar{\mathbf{K}}\Delta\bar{\mathbf{u}}_{n+1} - \bar{\mathbf{q}}\Delta\bar{\mu}_{n+1} = \mathbf{0}\,, \tag{54}$$

     where $\bar{\mathbf{K}}$ is the structural stiffness matrix. As the macroscopic previous state is defined, $\bar{\mathbf{r}}(\mathbf{0}, 0, \bar{\alpha}_n^i; \bar{\alpha}_n^i) = \mathbf{0}$ and the matrix $\bar{\mathbf{K}}$ is known, leading to $\Delta\bar{\mathbf{u}}_{n+1} = \bar{\mathbf{v}}\Delta\bar{\mu}_{n+1}$ with $\bar{\mathbf{v}} = \bar{\mathbf{K}}^{-1}\bar{\mathbf{q}}$. Using the arc–length constraint $\bar{h}(\Delta\bar{\mathbf{u}}_{n+1}, \Delta\bar{\mu}_{n+1}) = 0$, the quadratic equation in $\Delta\bar{\mu}_{n+1}$ is found to be

     $$\left(1 + \frac{\bar{\mathbf{v}}^T\bar{\mathbf{v}}}{\Psi^2}\right)\Delta\bar{\mu}_{n+1}^2 = \Delta L^2\,, \tag{55}$$

     leading to two possible solutions

     $$\Delta\bar{\mu}_{n+1} = \pm\frac{\Delta L}{A} \;\; \text{with } A = 1 + \frac{\bar{\mathbf{v}}^T\bar{\mathbf{v}}}{\Psi^2}\,. \tag{56}$$

   - The load parameter increment $\Delta\bar{\mu}$ takes one of two possible values above by following [30]:

     $$\begin{cases} \Delta\bar{\mu}_{n+1} = \frac{\Delta L}{A} & \text{if} \quad \bar{\mathbf{v}}^T\Delta\bar{\mathbf{u}}_n^{conv} \geq 0\,, \\ \Delta\bar{\mu}_{n+1} = -\frac{\Delta L}{A} & \text{if} \quad \bar{\mathbf{v}}^T\Delta\bar{\mathbf{u}}_n^{conv} < 0\,, \end{cases} \tag{57}$$

     where $\Delta\bar{\mathbf{u}}_n^{conv}$ is the displacement increment solution of the previous arc–length increment.

2. Convergence check step: Using the predicted displacement and load parameter, the macroscopic internal force is computed from the finite element approximation of Eq. (12). Note that during the force evaluation, the internal variables $\left(\bar{\alpha}_{n+1}^i\right)^k$ at iteration k are estimated from the displacement increment $\Delta\bar{\mathbf{u}}_{n+1}$ and from the converged internal variables at the previous step $\bar{\alpha}_n^i$, and not from the previous iteration in order to avoid any overload during the corrections, such that

   $$\left(\bar{\alpha}_{n+1}^i\right)^k = \bar{\mathfrak{A}}\left(\Delta\bar{\mathbf{u}}_{n+1}; \bar{\alpha}_n^i\right)\,, \tag{58}$$

which is governed by the material constitutive law. The macroscopic force residual $\bar{\mathbf{r}}$ is then estimated from Eq. (52) and the macroscopic convergence criterion is defined by

$$\bar{\varepsilon} = \frac{\|\bar{\mathbf{r}}\|}{\|\bar{\mathbf{f}}_{\text{int}}\| + \|\bar{\mathbf{q}}\bar{\mu}\|} < \text{Tolerance} . \tag{59}$$

If this condition is true, the next arc–length increment follows, else the corrector step is applied.

3. Macroscopic corrector step: $k = k + 1$

- The macroscopic force residual $\bar{\mathbf{r}}$ is successively linearized in terms of the displacement increment $\delta\bar{\mathbf{u}}^k$ and of the load parameter increment $\delta\bar{\mu}^k$ such that

$$\bar{\mathbf{r}}\left(\Delta\bar{\mathbf{u}}_{n+1} + \delta\bar{\mathbf{u}}^k, \Delta\bar{\mu}_{n+1} + \delta\bar{\mu}^k, \left(\bar{\alpha}_{n+1}^i\right)^k ; \bar{\alpha}_n^i\right) = \bar{\mathbf{r}}\left(\Delta\bar{\mathbf{u}}_{n+1}, \Delta\bar{\mu}_{n+1}, \left(\bar{\alpha}_{n+1}^i\right)^{k-1} ; \bar{\alpha}_n^i\right) + \bar{\mathbf{K}}^k\delta\bar{\mathbf{u}}^k - \bar{\mathbf{q}}\delta\bar{\mu}^k = \mathbf{0} , \tag{60}$$

where $\bar{\mathbf{K}}^k = \partial\bar{\mathbf{r}}\left(\Delta\bar{\mathbf{u}}_{n+1}, \Delta\bar{\mu}_{n+1}, \left(\bar{\alpha}_{n+1}^i\right)^{k-1} ; \bar{\alpha}_n^i\right)/\partial\bar{\mathbf{u}}$ is the stiffness matrix. Equation (60) thus leads to

$$\delta\bar{\mathbf{u}}^k = \bar{\mathbf{v}}^k\delta\bar{\mu}^k + \bar{\mathbf{d}}_r^k , \tag{61}$$

with $\bar{\mathbf{v}}^k = \left(\bar{\mathbf{K}}^k\right)^{-1}\bar{\mathbf{q}}$ and $\bar{\mathbf{d}}_r^k = -\left(\bar{\mathbf{K}}^k\right)^{-1}\bar{\mathbf{r}}$. By using Eq. (61), the arc–length constraint (51) $\bar{h}(\Delta\bar{\mathbf{u}}_{n+1} + \delta\bar{\mathbf{u}}^k, \Delta\bar{\mu}_{n+1} + \delta\bar{\mu}^k) = 0$ leads to a quadratic equation in $\delta\bar{\mu}^k$

$$A\left(\delta\bar{\mu}^k\right)^2 + B\delta\bar{\mu}^k + C = 0 , \tag{62}$$

where

$$A = 1 + \frac{\left(\bar{\mathbf{v}}^k\right)^T \bar{\mathbf{v}}^k}{\Psi^2} , \tag{63}$$

$$B = 2\left[\Delta\mu_{n+1} + \frac{\left(\bar{\mathbf{v}}^k\right)^T \left(\Delta\bar{\mathbf{u}}_{n+1} + \bar{\mathbf{d}}_r^k\right)}{\Psi^2}\right] \qquad \text{and} \tag{64}$$

$$C = \frac{\left(\Delta\bar{\mathbf{u}}_{n+1} + \bar{\mathbf{d}}_r^k\right)^T \left(\Delta\bar{\mathbf{u}}_{n+1} + \bar{\mathbf{d}}_r^k\right)}{\Psi^2} + \Delta\mu_{n+1}^2 - \Delta L^2 . \tag{65}$$

Equation (62) has two roots

$$\gamma_{1,2} = \frac{-B \pm \sqrt{B^2 - 4AC}}{2A} , \tag{66}$$

and the corrected increment $\delta\bar{\mu}$ takes one of these two values by following the argumentation of [30, 33]:

$$\begin{cases} \delta\bar{\mu}^k = \gamma_1 & \text{if} \quad (\Delta\bar{\mathbf{u}}_{n+1})^T \left(\gamma_2\bar{\mathbf{v}}^k + \bar{\mathbf{d}}_r^k\right) \leq (\Delta\bar{\mathbf{u}}_{n+1})^T \left(\gamma_1\bar{\mathbf{v}}^k + \bar{\mathbf{d}}_r^k\right) , \\ \delta\bar{\mu}^k = \gamma_2 & \text{if} \quad (\Delta\bar{\mathbf{u}}_{n+1})^T \left(\gamma_1\bar{\mathbf{v}}^k + \bar{\mathbf{d}}_r^k\right) < (\Delta\bar{\mathbf{u}}_{n+1})^T \left(\gamma_2\bar{\mathbf{v}}^k + \bar{\mathbf{d}}_r^k\right) . \end{cases} \tag{67}$$

- The displacement and load parameter increments are updated with the corrected values

$$\begin{cases} \Delta\bar{\mathbf{u}}_{n+1} = \Delta\bar{\mathbf{u}}_{n+1} + \delta\bar{\mathbf{u}}^k , \\ \Delta\bar{\mu}_{n+1} = \Delta\bar{\mu}_{n+1} + \delta\bar{\mu}^k . \end{cases} \tag{68}$$

- One can now go back to the convergence check step 2.

4.2. Solution of the microscopic BVP

At the micro–scale, the non–linear system (47) with the Lagrange multipliers λ must be solved.

Because of the linear independence of the linear constraints (46), the inversion of the matrix $\mathbf{CC}^T$ exists. Thus the Lagrange multipliers follow from the first equation of the non–linear system (47) multiplied by $\mathbf{C}$, yielding

$$\lambda = \left(\mathbf{CC}^T\right)^{-1}\mathbf{Cf}_{\text{int}} \,. \tag{69}$$

The Lagrange multipliers can then be eliminated from the internal force residual equation of the non–linear system (47), allowing the internal force residual to be defined as

$$\mathbf{0} = \mathbf{r} = \left[\mathbf{I} - \mathbf{C}^T\left(\mathbf{CC}^T\right)^{-1}\mathbf{C}\right]\mathbf{f}_{\text{int}} = \mathbf{Q}^T\mathbf{f}_{\text{int}} \,, \tag{70}$$

where $\mathbf{Q} = \mathbf{I} - \mathbf{RC}$ with $\mathbf{R}^T = \left(\mathbf{CC}^T\right)^{-1}\mathbf{C}$. Note that the matrices $\mathbf{Q}$ and $\mathbf{R}$ always exist. This equation is completed by the definition of the constraints residual

$$\mathbf{0} = \mathbf{r}_c = \mathbf{Cu} - \mathbf{g}_0 - \mathbf{q}\mu \,, \tag{71}$$

from the second equation of the non–linear system (47).

The system of equations (70, 71) is iteratively solved until satisfying the third equation of the non–linear system (47), *i.e.* the condition $\mu = 1$, which corresponds to satisfying the constrained macro–deformations. Indeed with a path following method the load parameter μ is also an unknown of the system. However in a multiscale framework, contrarily to the macro–scale case, the load parameter is no longer free of constraints at the micro–scale as the boundary condition of the microscale BVP is constrained strictly by the deformation gradient tensor and its gradient resulting from the macro–scale computation. This iterative procedure is described here below.

The linearized form, with respect to the displacement $\Delta\mathbf{u}$ and to the load parameter $\Delta\mu$, of the system (70, 71) is considered:

$$\mathbf{r} + \mathbf{Q}^T\mathbf{K}\Delta\mathbf{u} = \mathbf{0} \text{ and} \tag{72}$$

$$\mathbf{r}_c + \mathbf{C}\Delta\mathbf{u} - \mathbf{q}\Delta\mu = \mathbf{0} \,, \tag{73}$$

where $\mathbf{K} = \partial\mathbf{f}_{\text{int}}/\partial\mathbf{u}$ is the microscopic stiffness matrix. After some manipulations [48], the linearized form (72, 73) is found to be equivalent to

$$\tilde{\mathbf{r}} + \tilde{\mathbf{K}}\Delta\mathbf{u} - \tilde{\mathbf{q}}\Delta\mu = \mathbf{0} \,, \tag{74}$$

with

$$\tilde{\mathbf{r}} \ = \ \mathbf{r} + \left(\mathbf{C}^T - \mathbf{Q}^T\mathbf{KR}\right)\mathbf{r}_c \,, \tag{75}$$

$$\tilde{\mathbf{K}} \ = \ \mathbf{C}^T\mathbf{C} + \mathbf{Q}^T\mathbf{KQ} = \tilde{\mathbf{K}}(\mathbf{u}) \text{ and} \tag{76}$$

$$\tilde{\mathbf{q}} \ = \ \left(\mathbf{C}^T - \mathbf{Q}^T\mathbf{KR}\right)\mathbf{q} = \tilde{\mathbf{q}}(\mathbf{u}) \,, \tag{77}$$

where $\tilde{\mathbf{r}}$, $\tilde{\mathbf{K}}$ and $\tilde{\mathbf{q}}$ are the effective residual vector, stiffness matrix and load vector respectively.

For each iteration k of the macroscopic time step from time t_n to time t_{n+1} several time steps are required at the microscopic scale. We thus denote the iterations and steps at the micro–scale by respectively k' and n' to avoid any confusion. The microscopic state vector is defined by $[\mathbf{u}^T \ \mu]^T$. As the microscopic previous state $[\mathbf{u}_{n'}^T \ \mu_{n'}]^T$ is known, the microscopic current state $[\mathbf{u}_{n'+1}^T \ \mu_{n'+1}]^T$ must be computed by finding a displacement increment $\Delta\mathbf{u}_{n'+1}$ and a load parameter increment $\Delta\mu_{n'+1}$ such that

$$\mathbf{u}_{n'+1} \quad = \mathbf{u}_{n'} + \Delta\mathbf{u}_{n'+1} \text{ and} \tag{78}$$

$$\mu_{n'+1} \quad = \mu_{n'} + \Delta\mu_{n'+1} \,. \tag{79}$$

The non–linear system of equations (70, 71) is completed by an arc–length constraint

$$h(\Delta\mathbf{u}, \Delta\mu) = \frac{\Delta\mathbf{u}^T \Delta\mathbf{u}}{\psi^2} + \Delta\mu^2 - \Delta l^2 = 0, \tag{80}$$

where Δl is the arc–length increment step and where ψ is the constant parameter used to yield a non-dimensionless equation. The scale parameter ψ is set at the computation beginning by an arbitrary value which has the same magnitude as the resulting displacement. Finally, the non–linear system of equations related to the microscopic BVP for each iterative arc–length increment step is summarized as

$$\tilde{\mathbf{r}}(\Delta\mathbf{u}_{n'+1}, \Delta\mu_{n'+1}, \alpha_{n'+1}^i; \alpha_{n'}^i) = \mathbf{0} \text{ and} \tag{81}$$

$$h(\Delta\mathbf{u}_{n'+1}, \Delta\mu_{n'+1}) = 0. \tag{82}$$

where $\alpha_{n'+1}^i$ and $\alpha_{n'}^i$ are the microscopic internal variables (stress, strain, plastic deformation, *etc.*) at the time steps $n' + 1$ and n' respectively. The resolution of the system of equations (81, 82) for an arc–length interval $[l_{n'} \ l_{n'+1}]$ with $\Delta l = l_{n'+1} - l_{n'}$ follows the same predictor–corrector scheme as for the macroscopic BVP.

   For each macroscopic arc–length increment ΔL, the microscopic BVPs are iteratively solved until the microscopic solution corresponding to the prescribed macroscopic strains is obtained. The details of a typical iterative solution of a microscopic BVP is summarized as follows:

1. Receive the macroscopic deformation gradient $\bar{\mathbf{F}}$ and its gradient $\bar{\mathbf{G}}$ from the macroscopic BVP.
2. Assemble and parametrize the linear constraint (46).
3. Load the microscopic state reached at the end of the previous macro arc–length increment.
4. Adjust the arc–length increment Δl
5. Microscopic predictor step: The predictor of $\Delta\mathbf{u}_{n'+1}$ and $\Delta\mu_{n'+1}$ are computed using a similar procedure as for the macroscopic predictor, but by considering the effective stiffness $\tilde{\mathbf{K}}$ and the effective load vector $\tilde{\mathbf{q}}$ instead of the macroscopic stiffness and macroscopic load vector. $\tilde{\mathbf{K}}$ and $\tilde{\mathbf{q}}$ are computed from Eqs. (76) and (77).
6. Check convergence: From the estimated values of the displacement and load parameter increments, the effective residual $\tilde{\mathbf{r}}$ is computed. At each iteration index k', the internal variables $\left(\alpha_{n'+1}^i\right)^{k'}$ are estimated from the displacement increment $\Delta\mathbf{u}_{n'+1}^{k'}$ and from the converged internal variables at the previous time step $\alpha_{n'}^i$, such that

$$\left(\alpha_{n'+1}^i\right)^{k'} = \mathfrak{A}\left(\Delta\mathbf{u}_{n'+1}^k; \alpha_{n'}^i\right), \tag{83}$$

   which is governed by the material constitutive law. The convergence criterion is defined by

$$\varepsilon = \frac{\|\tilde{\mathbf{r}}\|}{\|\mathbf{f}_{\text{int}}\|} < \text{Tolerance}. \tag{84}$$

   If this condition is satisfied, step 8 follows, else step 7 follows.
7. Microscopic corrector step: The displacement increment $\delta\mathbf{u}^{k'}$ and the load parameter increment $\delta\mu^{k'}$ are computed using a similar procedure as for the macroscopic case by using the effective stiffness and the effective load vector instead of the macroscopic stiffness and macroscopic load vector. The displacement and load parameter increments are thus updated following

$$\begin{cases} \Delta\mathbf{u}_{n'+1} = \Delta\mathbf{u}_{n'+1} + \delta\mathbf{u}^{k'} \text{ and} \\ \Delta\mu_{n'+1} = \Delta\mu_{n'+1} + \delta\mu^{k'}. \end{cases} \tag{85}$$

8. Control parameter updating step: $\mu_{n'+1} = \mu_{n'} + \Delta\mu_{n'+1}$.
   (a) If $\mu_{n'+1} \leq 1$,
      - Update the displacement vector $\mathbf{u}_{n'+1} = \mathbf{u}_{n'} + \Delta\mathbf{u}_{n'+1}$.
      - Compute and store the stress field corresponding to the current state.
      - If $\mu_{n'+1} < 1$, assign the current state to the previous one and go to step. 4.

- If $\mu_{n'+1} = 1$, go to step 9.

(b) Else if $\mu_{n'+1} > 1$, the last microscopic increment reaches a point beyond the constrained boundary conditions arising from the macro-scale problem and the last computed micro–scale step $n' + 1$ has to be recomputed from the previous converged micro–scale step n' by considering a new load increment $\Delta l = \Delta \mu = 1 - \mu_{n'}$. The size of this new increment is obtained using an iterative conventional Newton–Raphson step in order to obtain the exact condition $\mu = 1$. Note that we cannot simply unload from the last converged micro–scale step to reach $\mu = 1$ in case of irreversible behaviors. Then go to step 4.

9. Final step: The homogenized stresses and the homogenized tangents are estimated from the microscopic solution, see [27].
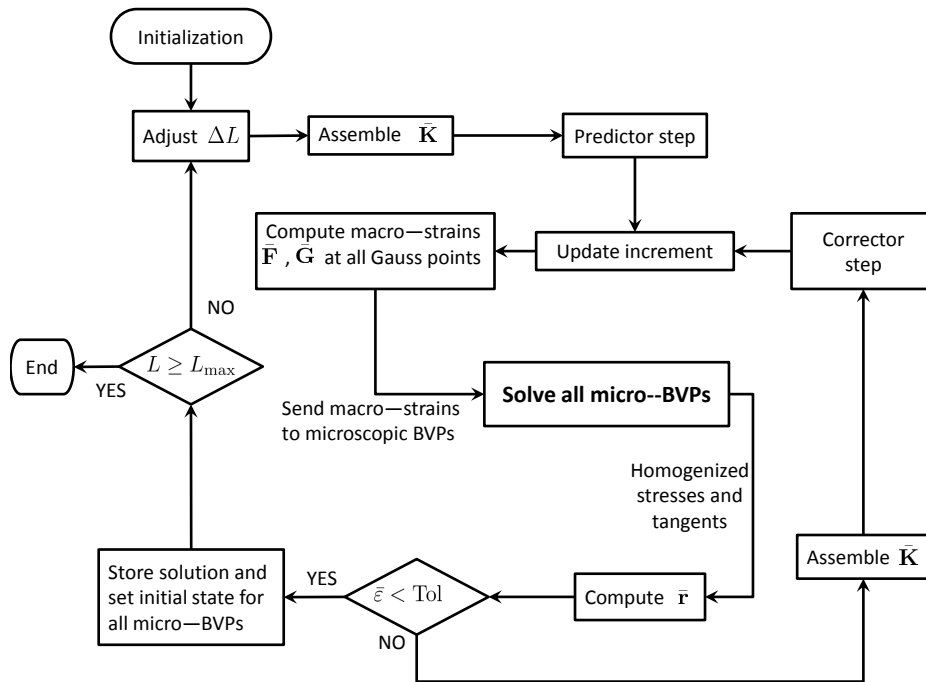
Figure 5. Multi–scale computation with path following method. The "micro–solver" block computes the homogenized stresses and tangent operators corresponding to the prescribed macroscopic strains.

This multi–scale computation methodology is schematized in Fig. 5. The micro–solver block is detailed in Fig. 6. The "initialization block" allows parallel simulations, see details in Appendix B. The parallel strategy is applied on both scales. At the macroscopic scale the mesh is partitioned on several processors. At the microscopic scale each microscopic BVP is solved in serial, but as a large number of microscopic BVPs are considered for each macro–scale processor, the microscopic BVPs of a macro–scale partition are distributed to different processors. This parallelization on a double level is summarized in Appendix B.

5. Numerical applications

In this section, the behavior of an hexagonal honeycomb structure under compression loading is studied by the proposed DG–based homogenization multi–scale framework. At first, to demonstrate the ability of the polynomial interpolation method to enforce the periodic boundary condition for cellular materials, a simple compression test of a particular RVE is considered. First, the effect of the interpolation order is examined when extracting the elastic homogenized properties corresponding to null macroscopic strains. Then, this microscopic BVP is solved by the path following method with the presence of microscopic bucking, which might lead to the macroscopic loss of ellipticity. Next, multi–scale simulations of a compression test of a plate made of this cellular material are conducted. For this
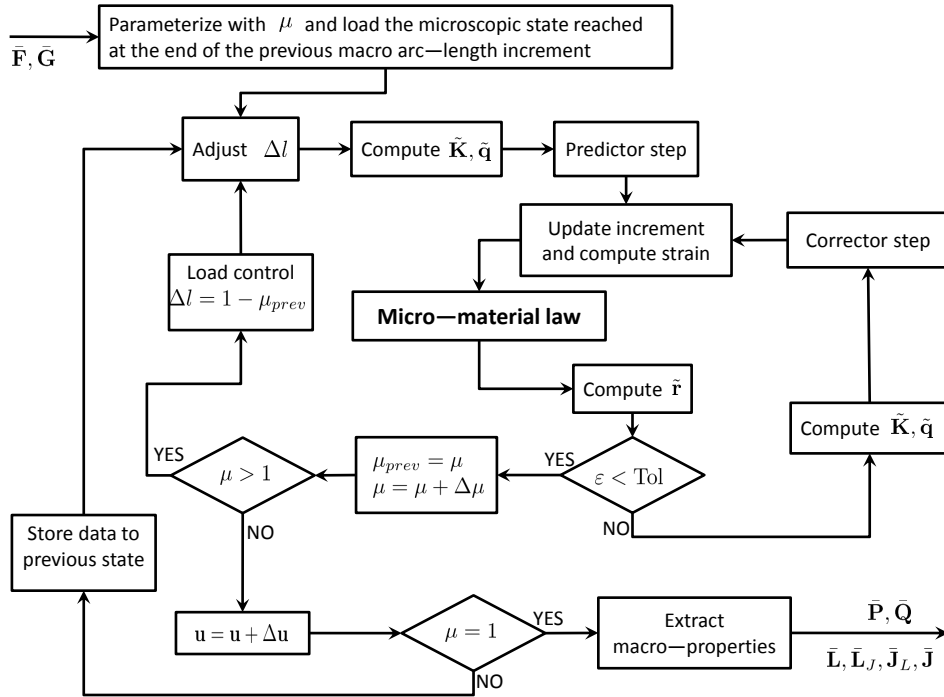
Figure 6. Details of micro–solver block.

test of reduced dimensions, the result of a direct numerical simulation is available and is used to demonstrate the accuracy of the multi–scale method and its non–dependency with the mesh size. A comparison of the memory and CPU time requirements is also provided. The choice of the RVE size on the results is then discussed as well as the effect of the imperfections in the honeycomb structure. Finally, a compression test of a center–hole plate is performed in order to show the efficiency of this multi–scale framework for larger problems. For this test, the direct numerical simulations could only be achieved using a high–memory computing node.

5.1. Definition of the hexagonal honeycomb structure

In the following numerical applications we consider the behavior of an hexagonal honeycomb structure. The perfect structure is characterized by the cell wall length $l = 1$ mm and the thickness $t = 0.01$ mm as depicted in Fig. 7 (left). The repeated unit (RU) is defined as the smallest repeated pattern as shown in Fig. 7 (right). In order to govern the microscopic buckling patterns, a small random disturbance is added into the perfect structure with a perturbation parameter δ, see Appendix C for details. The value of δ can vary to obtain different levels of the structure imperfection. The structure porosity is about 89%. The honeycomb structure is supposed to be infinitely long in the transverse direction so the plane strain state, in which $\partial u_i / \partial X_2 = 0$ with $i = 0, 1, 2$, is considered.

The cell walls obey to a $J2$-hyperelastic–based elasto–plastic material law formulated in large strains, see Appendix A for details of this material model. The material parameters are $K = 67.55$ GPa, $G = 25.9$ GPa, $\sigma_y^0 = 276.0$ MPa and $h = 6890.0$ MPa where K is the initial bulk modulus, G is the initial shear modulus, σ_y^0 is the initial yield stress and h is the hardening parameter.

5.2. Second–order periodic boundary condition with polynomial interpolation method

This section shows the efficiency of the polynomial interpolation method to enforce the periodic boundary condition for cellular materials. For this purpose we consider a 2x2–RU RVE (see Fig. 7 for the repeated unit – RU – definition) as an example, which is extracted from the hexagonal honeycomb structure described in section 5.1 with the perturbation parameter $\delta = 5\%$ (see Appendix C for details). Quadratic 6–node triangles with 3 Gauss points are used to discretize the problem, see Fig. 8. The vertical and horizontal sizes of the RVE are equal to 3.46 mm
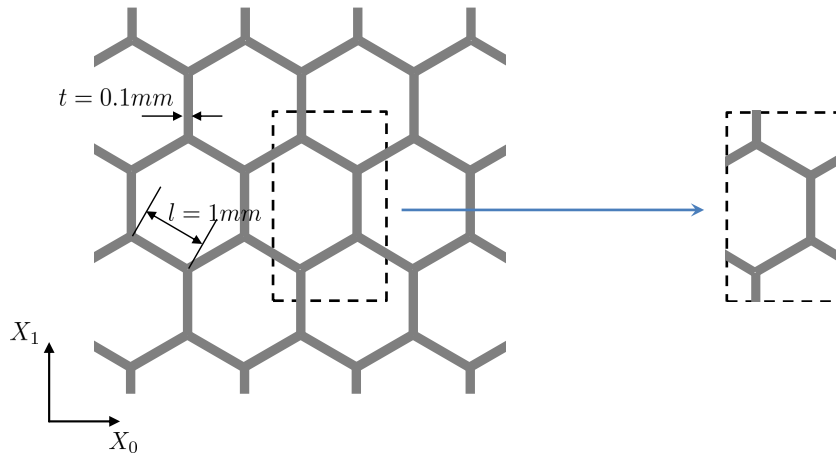
Figure 7. Perfect hexagonal honeycomb structure of cell wall length $l = 1$ mm and cell wall thickness $t = 0.1$ mm (left) and a repeated unit (RU) (right) containing 2 honeycomb cells. The RU width is $l\sqrt{3}$ and the RU height is $3l$.

and 6 mm respectively. The use of an imperfect structure leads to a non–conformal mesh, so the periodic boundary condition enforcement based on the matching nodes of two opposite boundaries cannot be used, motivating the use of the polynomial interpolation method. In this section, the 2x2–RU RVE is chosen as an example to demonstrate the
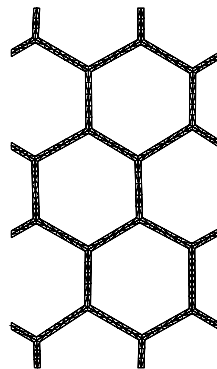
Figure 8. Finite element mesh of a 2x2–RU RVE (including 4 RUs presented in Fig. 7) of width 3.46 mm and of height 6.0 mm, with wall length $l = 1$ mm and wall thickness $t = 0.1$ mm. A perturbation of 5% is considered.

ability of the polynomial interpolation method to capture the deformed shapes of the cellular material. The effect of the RVE size on the two–scale computations will be discussed in the coming application.

5.2.1. Effect of the interpolation order

In this section, we consider the effect of the interpolation order for two kinds of interpolant functions: the Lagrange functions, in which case the interpolant order is the polynomial order, and cubic splines, in which case the interpolant order is the number of segments, refer to [42] for implementation details. To this end we study the initial elastic homogenized tangent operators, i.e. for the macroscopic deformation gradient $\bar{\mathbf{F}} = \mathbf{I}$ and its gradient $\bar{\mathbf{G}} = \mathbf{0}$, of the RVE. The homogenized tangent operators are computed using a condensation procedure from the microscopic stiffness matrix as presented in [27].

Figures 9a and 9b show the convergence of some components of the homogenized tangent operators in terms of the number of interpolant degrees of freedom in the cases of the Lagrange and of the cubic spline interpolation formulations. The convergence of L_{0000} and L_{1111} of the first–order tangent $\bar{\mathbf{L}} = \partial\bar{\mathbf{P}}/\partial\bar{\mathbf{F}}$ is plotted in Fig. 9a. The convergence of J_{000000}, J_{111111}, J_{001001} and J_{101101} of the second–order tangent $\bar{\mathbf{J}} = \partial\bar{\mathbf{Q}}/\partial\bar{\mathbf{G}}$ is plotted in Fig. 9b. A

larger interpolation order (Lagrange polynomial order or number of segments of the cubic spline) corresponds to a lower constraint on the system, and leads to the upper–bound convergence. For this RVE, a polynomial order larger than 9 (6+4×(9-1) = 38 dofs in 2D) or a number of segments larger than 2×5 along the two directions (6 + 4×5+4×2= 34 dofs) provides a converged estimation which is better than the results evaluated by the linear displacement boundary condition. This case corresponds to the polynomial order 1 and is given as the first points of the Lagrange interpolation curves, see Figs. 9a and 9b.
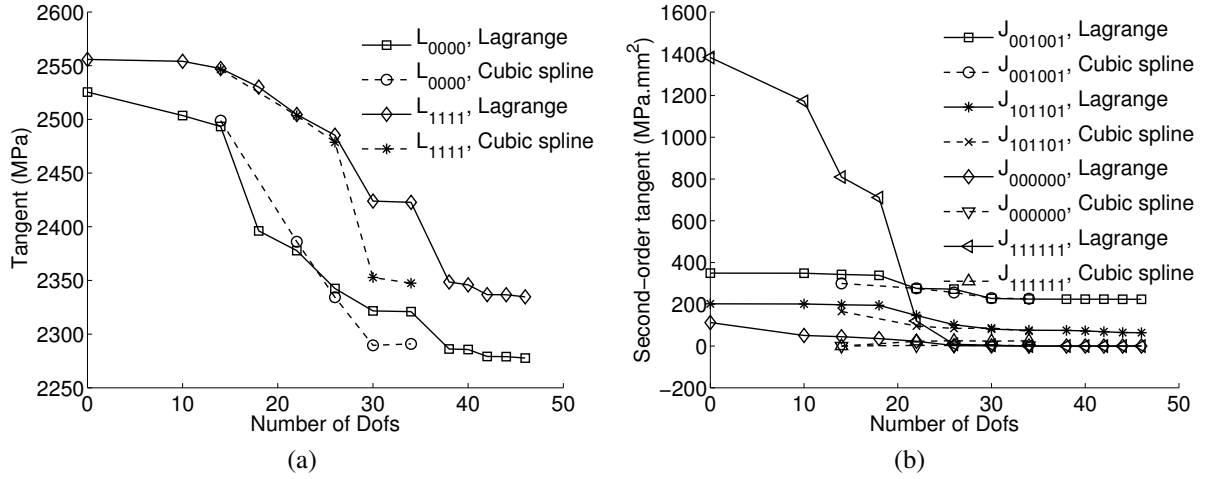
Figure 9. Convergence of the elastic homogenized properties in terms of the number of interpolant degrees of freedom added to the system: (a) convergence of some first–order tangent components and (b) convergence of some second–order tangent components. The first–order tangent is defined by $\bar{L}_{ijkl} = \frac{\partial \bar{P}_{ij}}{\partial \bar{F}_{kl}}$ and the second–order tangent is defined by $\bar{J}_{ijkpqr} = \frac{\partial \bar{Q}_{ijk}}{\partial \bar{G}_{pqr}}$.

This section considers an hexagonal honeycomb but this methodology can be easily derived to other kinds of structures. For 3-dimensional cellular structures, an arbitrary 3–dimensional interpolation method can be used, for example the patch Coons interpolation [42] and its implementation is directly extended from the 2–dimensional case.

5.2.2. Stability analysis of the microscopic problem

In this section, prescribed macroscopic strains are used to enforce a vertical compression. The prescribed macroscopic deformation gradient reads

$$\bar{\mathbf{F}} = \begin{bmatrix} 1 & 0 & 0 \\ 0 & 0.98 & 0 \\ 0 & 0 & 1 \end{bmatrix}, \tag{86}$$

and its gradient $\bar{\mathbf{G}} = \mathbf{0}$. This macroscopic strain state is parametrized by a unique control parameter $\mu \in [0\ 1]$ with

$$\bar{\mathbf{F}}_{\mu} = \mathbf{I} + \mu\left(\bar{\mathbf{F}} - \mathbf{I}\right) \text{ and} \tag{87}$$

$$\bar{\mathbf{G}}_{\mu} = \mu\bar{\mathbf{G}} = \mathbf{0}. \tag{88}$$

To constrain the PBC, the Lagrange interpolation of degree 9 for both horizontal and vertical directions is used as justified in Fig. 9. Beside using the elasto–plastic material law presented in Section 5.1, an elastic material law is also considered for comparison purpose. Because of the presence of non–linearities, an iterative Newton–Raphson solver is used at each increment of the control parameter. The homogenized stresses and homogenized tangents are estimated at each control step.

Figure 10 illustrates the homogenized Piola–Kirchhoff stress norm given by $\|\bar{\mathbf{P}}\| = \sqrt{\bar{\mathbf{P}} : \bar{\mathbf{P}}}$, with respect to the control parameter for both the elastic and the elasto–plastic cases. For the elastic case, the tangent values always remain positive but become close to 0 with the occurrence of microscopic buckling, as depicted in Fig. 11a. For
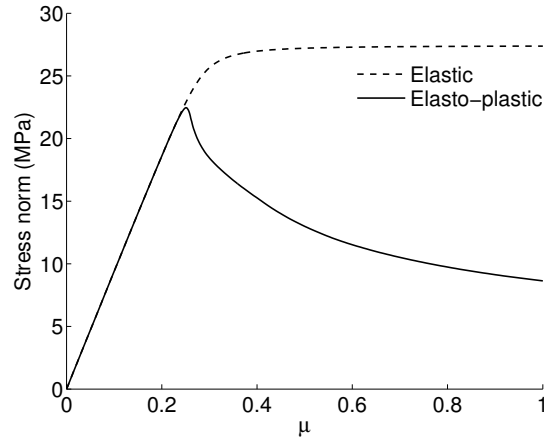
Figure 10. Comparison of the homogenized stress *vs.* strain relation for the elastic and elasto–plastic cases. The stress norm is defined by $\|\bar{\mathbf{P}}\| = \sqrt{\bar{\mathbf{P}} : \bar{\mathbf{P}}}$.
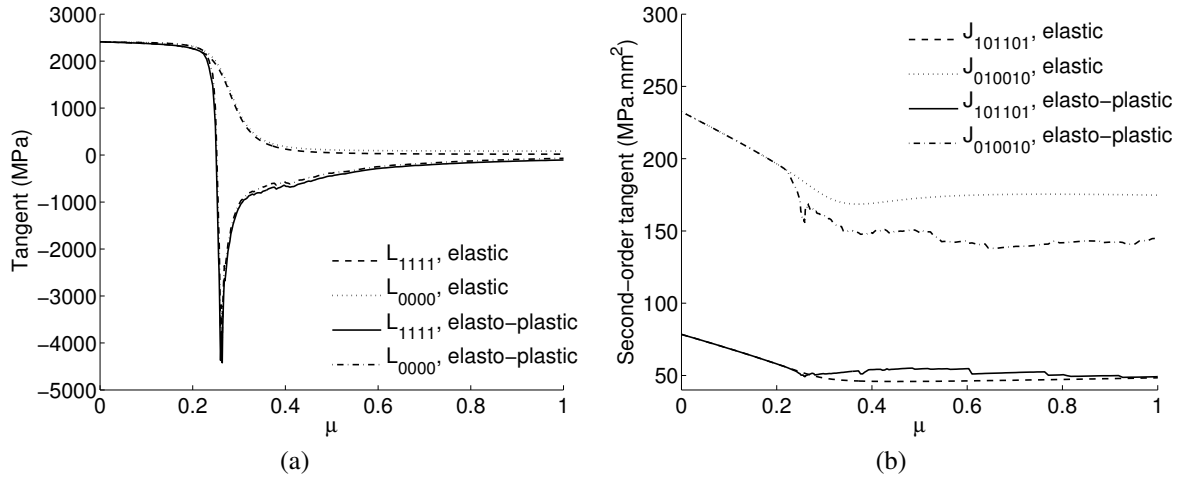

Figure 11. Comparison of the homogenized properties for the elastic and elasto–plastic problems: (a) first–order tangent components and (b) second–order tangent components.

the elasto–plastic case, the structure degradation is observed. The secondary path has a negative tangent. These negative tangent values are detailed in Fig. 11b. With a classical continuum, the presence of this softening part in the elasto–plastic case might lead to the appearance of a mesh–dependent localization. In the second–order multi–scale model used, the Mindlin strain gradient continuum is used at the macroscopic scale so that the macroscopic localization is expected to be captured under the form of bands independent of the mesh size by accounting for the positive second–order tangents, see Fig. 11b.

Finally, Figs. 12a and 12b show the buckling shape for both the elastic and the elasto–plastic cases at the last control step which corresponds to the prescribed macroscopic strains.

5.3. Multi–scale compression of a honeycomb structure

This section demonstrates the ability of the second–order DG–based multi–scale computational homogenization technique presented in Section 2 to study the behavior of structures made of cellular materials, for which the bucking occurs at the micro–scale leading to a macroscopic deformation localization. For this purpose we consider a uni–axial compression test of the hexagonal honeycomb structure presented in Section 5.1. The effects of the macro–mesh discretization, of the RVE size, and of the imperfection parameter δ are successively studied.
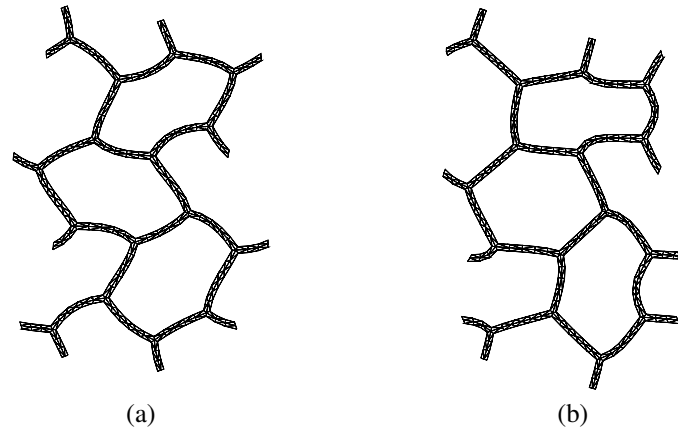
Figure 12. Buckling of the cell walls due to the vertical compression: (a) elastic buckling and (b) elasto–plastic buckling. The deformed shapes are presented.
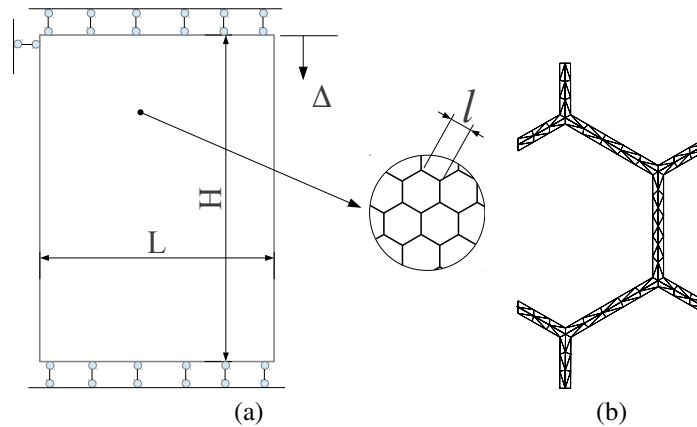

Figure 13. Uni–axial compression test: (a) macroscopic boundary condition for the uni–axial compression test and (b) repeated unit (RU).

Let us consider a structure of width $L = 65.8$ mm and of height $H = 101$ mm which is made of the hexagonal honeycomb presented in section 5.1, see Fig. 13, and constrained with the macroscopic boundary condition illustrated in Fig. 13a. The prescribed vertical displacement Δ is applied to the top boundary while the bottom is constrained vertically. The left and right boundaries are free to move. The horizontal displacement of a point on the left boundary is also fixed in order to prevent the rigid body motion. In order to trigger the macroscopic localization, a small random perturbation with $\delta = 1\%$ is introduced at the micro–scale, see Appendix C for details on adding the structure imperfection.

5.3.1. Study of the macro–mesh effect

First a direct simulation is carried out in which the whole structure made of discrete cell walls is meshed. The finite element mesh comprises 160820 quadratic 6–node triangles with 396258 nodes. The problem is solved by a standard arc–length path following technique as presented in Section 4. The results of this direct modeling are considered as a reference solution.

The multi–scale analyzes are performed by using the proposed DG–based second–order multi–scale computational homogenization scheme presented in Section 2. To evaluate the absence or not of the macroscopic mesh size effect, three finite element meshes of quadratic 9–node quadrangles are used, as shown in Fig. 14. These meshes are respectively noted as (i) mesh 0, (ii) mesh 1 and (iii) mesh 2. A series of 500 repeated units (RUs) with a random perturbation $\delta = 1\%$ is chosen to construct the mesh library of the RVEs. This choice is motivated by the fact that
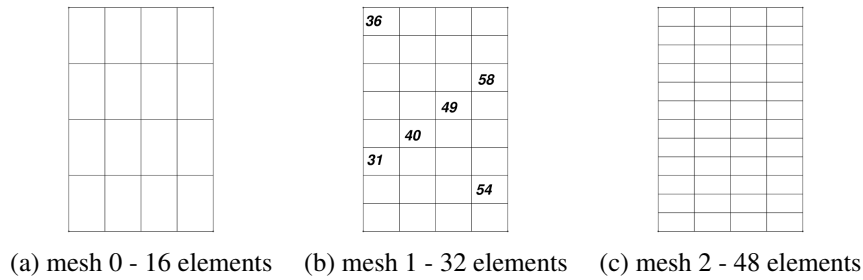
(a) mesh 0 - 16 elements　　　(b) mesh 1 - 32 elements　　　(c) mesh 2 - 48 elements

Figure 14. Macroscopic meshes used in the simulations. Some elements are noted in order to follow the deformation of the micro–structure during loading.

Method	CPU time per iteration	Used memory
Full model	92 seconds	5.6 gigabytes
Multi–scale model, mesh 0	36 seconds	1.3 gigabytes
Multi–scale model, mesh 1	84 seconds	2.6 gigabytes
Multi–scale model, mesh 2	146 seconds	4.0 gigabytes

Table 1. Computation time and used memory of the full model and multi–scale models. These computations were performed in the same machine with one processor.

a single unit contains all the statistical information of the micro–structure (for low imperfection). The cell walls are meshed with quadratic 6–node triangles, see Fig. 13b. The presence of imperfections in each RVE leads to non–conformal meshes that motivates the use of the polynomial interpolation method. The Lagrange interpolation is adopted here with a degree of 4 in the horizontal direction and of 9 in the vertical direction. Note that in the multi–scale computational method, the underlying macroscopic and microscopic meshes are independent since the scale transition is only guaranteed through microscopic volume integrals.
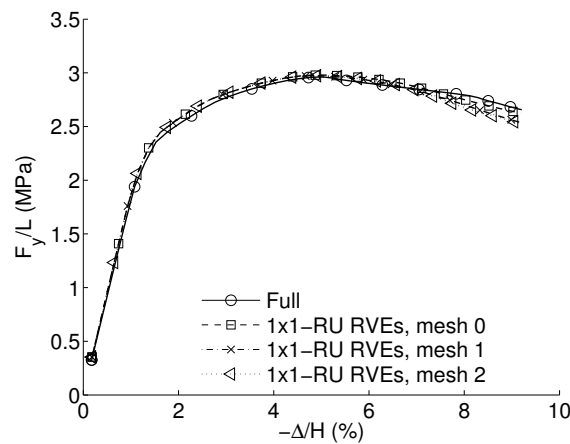

Figure 15. Vertical reaction force *vs.* relative displacement curves obtained with the second–order multi–scale scheme. The solution from the direct numerical simulation is also reported.

Figure 15 shows the vertical macroscopic reaction force curves in terms of the relative displacement obtained for the three meshes of the macroscopic structure and for the reference solution obtained with the direct numerical simulation. A good agreement between the multi–scale and the reference results is observed. Because of the second–order scheme, the results are quasi–independent of the mesh size despite the localization band. Before the localization onset stated by the maximal force in the force–displacement curves, this multi–scale approach over–estimates slightly the results compared to the reference solution. After this point, it slightly under–estimates the curves. This point

can be explained by the fact that the occurrence of the microscopic buckling leads to strong fluctuations in the field over the microscopic structure, and that the quadratic distribution of the macroscopic displacement field (linear in deformation) is only an approximation that cannot capture this high order effect.
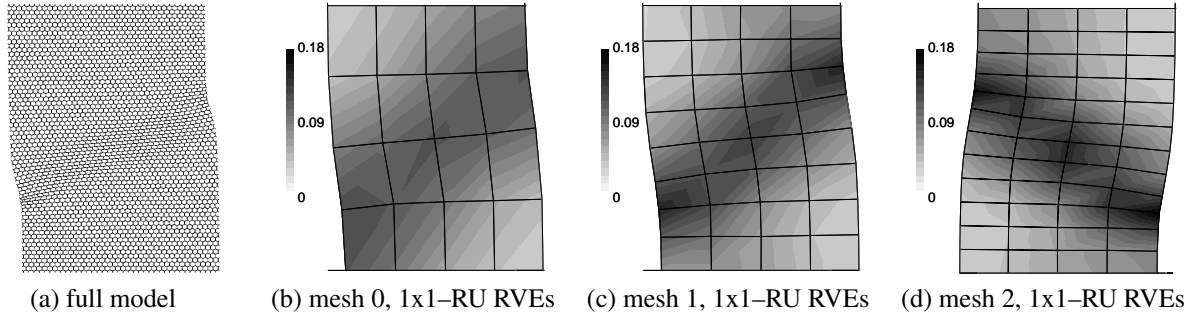

| (a) full model | (b) mesh 0, 1x1–RU RVEs | (c) mesh 1, 1x1–RU RVEs | (d) mesh 2, 1x1–RU RVEs |

Figure 16. Deformation shape obtained with the direct simulation (a) and distributions of the equivalent Green–Lagrange strain obtained with the multi–scale simulations for (b) the mesh 0, (c) the mesh 1 and (d) the mesh 2. The equivalent Green–Lagrange strain is given by $\bar{e}_{GL} = \sqrt{\frac{2}{3}\mathrm{dev}(\bar{\mathbf{E}}) : \mathrm{dev}(\bar{\mathbf{E}})}$, where $\mathrm{dev}(\bullet)$ is the deviatoric operator and where $\bar{\mathbf{E}} = \frac{1}{2}\left(\bar{\mathbf{F}}^T\bar{\mathbf{F}} - \mathbf{I}\right)$.

Figure 16a shows the deformed shape predicted with the direct simulation of the full–model problem and Figs. 16b, c, d, show the distribution of the equivalent Green–Lagrange strain obtained with the multi–scale simulations and the different meshes. Clearly, as for the force–displacement curves, the macroscopic strain distribution patterns in Figs. 16b, 16c and 16d are weakly dependent on the mesh size. The deformation pattern of the direct simulation is captured by the multi–scale simulations and one can conclude that the second–order scheme provides an acceptable solution with a lower number of degrees of freedom.

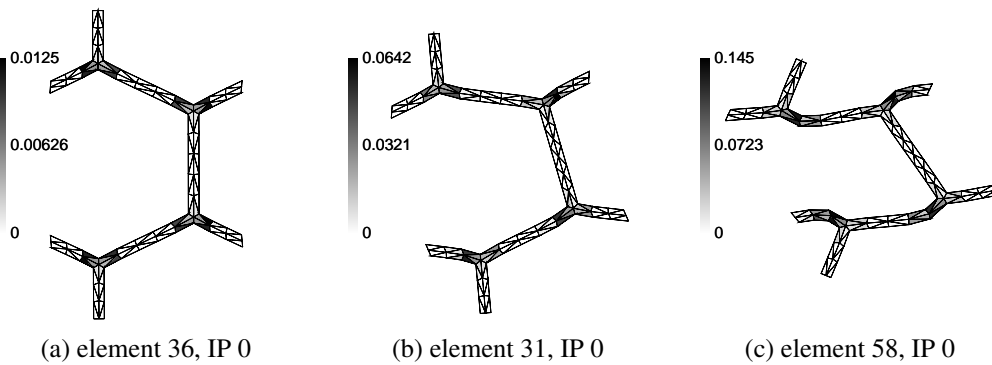| (a) element 36, IP 0 | (b) element 31, IP 0 | (c) element 58, IP 0 |

Figure 17. Equivalent plastic strain distributions and plastic hinges at different locations of the macro–mesh.

Figure 17 illustrates the final distribution of the equivalent plastic strain obtained for micro–structural problems at different Gauss points of the macro–scale mesh 1. The locations of the Gauss points are identified on Fig. 14b. As expected, the microscopic structure deforms more inside the localization band (elements 31 and 58 at Gauss point 0) and less outside (element 36 at Gauss point 0). Figure 18 depicts the evolution of the homogenized stress component $\bar{P}_{11}$ in terms of the vertical deformation $1 - \bar{F}_{11}$ at different Gauss points of the mesh 1. The strain softening stages are clearly observed at the different locations. Finally the evolutions of the homogenized second–order stress norm at different Gauss points of the macro–scale mesh 1, in terms of the macroscopic compression displacement, are reported in Fig. 19. Clearly the second–order stress becomes more important after the onset of localization.

The comparison of the computational resources required to conduct the full direct numerical simulation and the different multi–scale simulations are reported in Tab. 1. For this comparison, all the simulations were conducted on a single processor. Despite the simplicity of the problem, the full direct numerical simulation requires more than 5 gigabytes of memory due to the size of the stiffness matrix to be solved. The multi-scale approach always requires less memory. When considering the multi–scale approach, the mesh 0 and mesh 1, see Fig. 14, require a
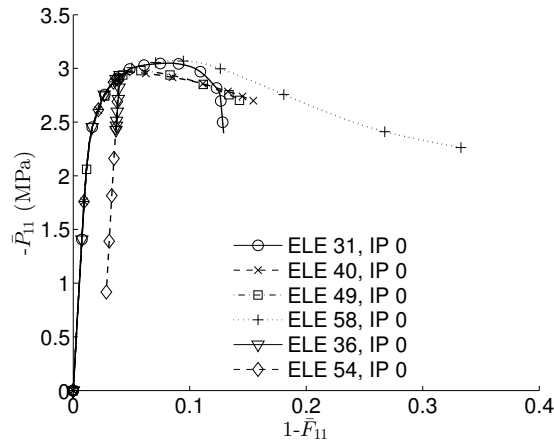
Figure 18. Homogenized stress $\bar{P}_{11}$ *vs.* vertical deformation $1 - \bar{F}_{11}$ at different Gauss points of the mesh 1.
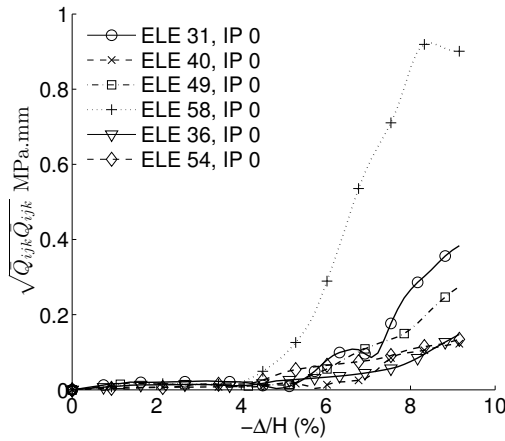

Figure 19. Homogenized second–order stress norm $\sqrt{\bar{Q}_{ijk}\bar{Q}_{ijk}}$ *vs.* the prescribed displacement Δ at different Gauss points of the mesh 1.

lower computational (CPU) time than the direct numerical resolution. The resolution of the finest macroscopic mesh, mesh 2, is slower due to the higher number of microscopic problems. Note that in general, if the dimensions of the macroscopic problem increase with respect to the size of the micro–structure, here the honeycomb structure, the computational time and the used memory of the full model largely increase. As the resolution of large systems is still a challenge with actual modern computers, the use of multi–scale models becomes much more efficient than the direct numerical simulations as it will be the case for the next example. Moreover, for the multi–scale approach the computational resources depend more on the number of microscopic problems to be solved than on the size of the stiffness matrix of the macroscopic problem. Thus for parallel simulations, the multi–scale problem can be partitioned more efficiently as the computational requirement does not result from a single matrix storage and resolution but from the number of different microscopic problems to be solved.

5.3.2. Study of the RVE size effect

With a second–order computational homogenization scheme, the size of the RVEs directly relates to the characteristic length scale of the Mindlin strain gradient continuum as stated in [49]: a larger size of the RVE leads to a larger characteristic length. In order to analyze the influence of the RVE size on the multi–scale results, five different RVEs are successively considered –1x1–RU, 2x2–RU, 2x1–RU, 1x2–RU, and 3x3–RU– for the multi–scale analysis using the macroscopic mesh 1 presented in Fig. 14b. Note that the size of a RU refers to the micro–structure, without

(a) overall response
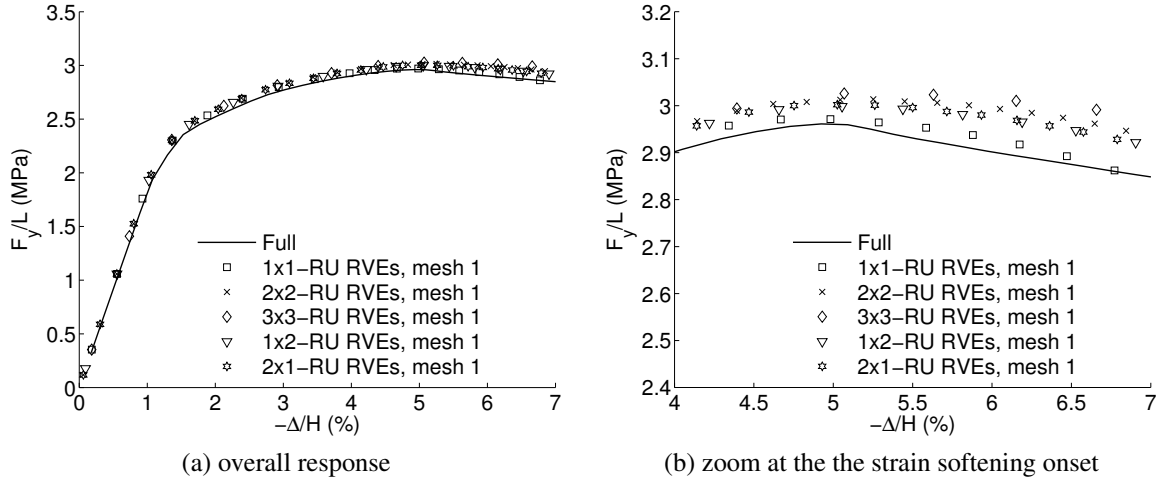
(b) zoom at the the strain softening onset

Figure 20. Vertical reaction force *vs.* relative compression displacement obtained by the second–order homogenization scheme for different RVE sizes. The solution from the direct simulation is also shown.
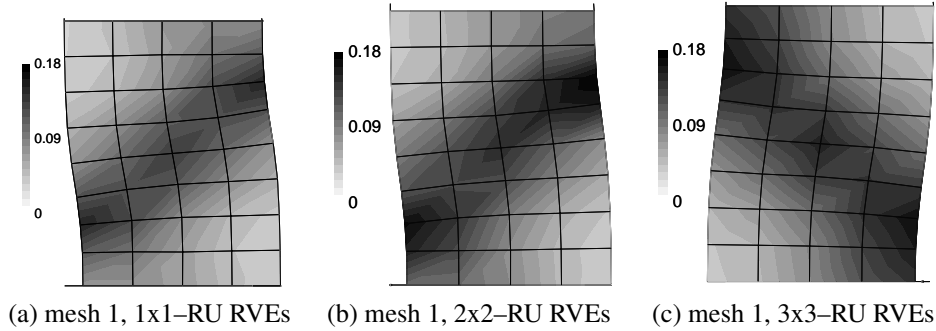

(a) mesh 1, 1x1–RU RVEs   (b) mesh 1, 2x2–RU RVEs   (c) mesh 1, 3x3–RU RVEs

Figure 21. Equivalent Lagrange strain distribution obtained by multi-scale simulations using different RVEs: (b) mesh 1, 1x1–RU RVEs, (c) mesh 1, 2x2–RU RVEs and (d) mesh 1, 3x3–RU RVEs.

perturbation, of width $l\sqrt{3}$ and of height $3l$,in which l is the length of the honeycomb edge.

The reaction forces in terms of the relative compression displacement obtained for the five simulations are reported in Fig. 20 and are compared with the reference solution obtained by the direct numerical simulation. During the elastic response the solution does not depend on the RVE size as the strain is uniform (there is thus no length scale effect). When the micro-buckling appears, the existence of a strain gradient leads to a size effect and it can be seen on Fig. 20b that, with the multi-scale scheme, the predicted strain softening onset increases slightly with the size of the RVE as expected (the increase of the strain softening onset is about 3% for an increase of the RVE size from 1x1 to 3x3). The strain softening onset predicted with the 1x1–RU is the closest to the one predicted with the direct numerical simulation. During the strain softening response the localization band induces a higher strain gradient in the structure and the RVE size modifies the slope of the response. This was also expected as under a strain gradient the response depends on the characteristic length. This behavior was studied in the non-local damage model litterature, *e.g.* [50], in which a material length scale is defined to capture the localization bands and the strain softening response due to damage. In our context of a second–order computational homogenization, the material length scale is directly related to the size of the RVE [49] and the localization band results from the micro–bucklings, but the behavior is similar. Figure 20b illustrates that compared to the direct numerical simulation results, the force is slightly overestimated during the softening response for the larger RVE sizes (within 5%). Finally the distributions of the equivalent Lagrange strain obtained with 1x1–RU, 2x2–RU, and 3x3–RU RVEs are shown in Fig. 21. The width of the localization pattern is slightly increased when the RVE size becomes larger, which is in agreement with the reduction of the strain softening effect observed in Fig. 20b.

From this analysis, it appears that the selection of the RVE as a single RU seems more appropriate on the accuracy point of view, but also because the computation cost is much lower. We will now assess this selection by considering the compression of honeycomb plates of different dimensions, so with different characteristic length *vs.* macro–size ratios. Indeed, it was shown in the literature that the cell size in cellular materials acts as a characteristic material length scale and that the behavior of macroscopic structures can exhibit a size effect, see *e.g.* [2]. This size effect in cellular materials can be captured using the generalized continuum, see *e.g.* [51]. In our approach, the size effect during the localization is expected to be captured using the second–order multi–scale computational homogenization framework in which the Mindlin strain gradient is considered at the macroscopic scale (the Mindlin strain gradient formulation has been used to account for the size effects for both elasticity, see *e.g.* in [52], and elasto–plasticity, see *e.g.* [53]).
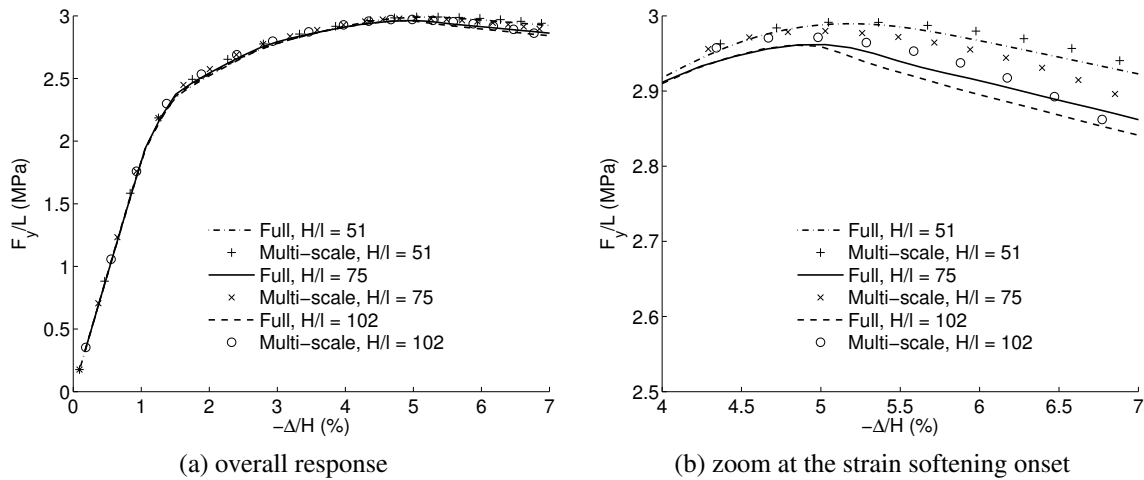

Figure 22. Vertical reaction force *vs.* relative compression displacement obtained by the second–order homogenization scheme for different plate. The solution from the direct simulation is also shown.

By increasing proportionally the width and height of the honeycomb plate while keeping constant the honeycomb cell size allows studying the influence of the ratio between the plate dimensions and the cell size. Three different ratios, $H/l = 51$, $H/l = 75$ and $H/l = 102$ are successively considered with the multi–scale analysis using the macroscopic mesh 1 presented in Fig. 14b and with the 1x1–RU RVE. The structural responses are compared with direct numerical simulations in Fig. 22. Although small, the size effect is observed in the strain softening onset prediction and in the strain softening regime. The same trend is observed for the direct and multiscale simulations: the strain softening onset happens later for smaller macroscopic sizes. The multi–scale predictions lie within 1% of the direct numerical results.

This study justifies the use of a 1x1–RU RVE to capture correctly the strain softening onset and the softening response while keeping a reduced computational cost.

5.3.3. Study of the imperfection degree effect

From the above examples, we can conclude that the second–order computational homogenization technique can be used for cellular materials. The size of the RVEs within this scheme is limited by the fact that the use of larger sizes of the RVEs leads to larger length scales of the macroscopic Mindlin strain gradient continuum [49] and leads to over–estimate the results. Using a small RVE size is acceptable for honeycomb materials as a single repeated unit remains representative. For random micro–structures, choosing a small RVE size potentially leads to large variations of the homogenized properties. A compromise should thus be made. As an illustration results obtained with different levels of imperfection ranging from a quasi-perfect micro–structure –for which a single repeated unit is representative– to a 30 % imperfect micro–structure –for which this is no longer the case– are reported in Fig. 23. These results are obtained by using the macroscopic mesh 1, see Fig. 14, and a single repeated unit at the microscopic level. A larger value of the perturbation δ leads to a softer result on the macroscopic force–displacement behavior, which is not necessarily physical. Thus this approach cannot be used for structures with high degrees of imperfection, but is
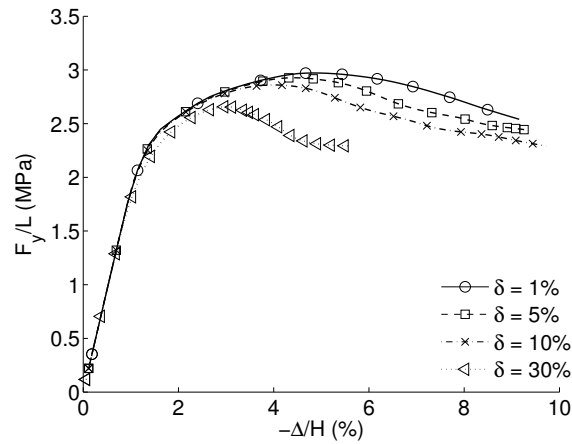
Figure 23. Effect of the imperfection level δ. The results are obtained with the mesh 1 and 1x1–RU RVEs.

shown to predict with accuracy the behavior of structure made of regular micro–patterns for which a single RU can be considered as a RVE.

5.4. Multi–scale compression of a rectangular plate with a central hole

In this section, the proposed DG–based second–order multi–scale computational homogenization approach is applied to consider the behavior of a rectangular plate with a central hole made of the elasto–plastic honeycomb structure presented in section 5.1. The micro–structure is characterized by a cell wall length $l = 1$ mm, a cell wall thickness $t = 0.1$ mm and a perturbation parameter $\delta = 1\%$ in order to initiate the microscopic buckling patterns.

At the macroscopic scale, the homogeneous model of the plate is considered. The radius of the central hole is denoted by $r = 15$ mm. The height and width of this plate are $H = 180$ mm and $L = 90$ mm respectively. The macroscopic geometry and the macroscopic boundary conditions are illustrated in Fig. 24a. The macroscopic problem is discretized by quadratic 6–node triangles and quadratic 9-node quadrangles as shown in Fig. 24b. The full model is also considered with 297739 quadratic 6–node triangles with 732082 nodes in order to compare to the multi-scale model.

For the microscopic analyzes, as justified in the previous application, the 1x1–RU of width 1.73 mm and height 3 mm can be used as a RVE. In order to account for the imperfection, a library of 500 random RVEs with an imperfection $\delta = 1\%$ is generated. The cell walls are meshed with quadratic 6–node triangles, see Fig. 13b. The Lagrange interpolation is adopted here with the degrees of 4 in the horizontal direction and of 9 in the vertical direction.

Fig. 25a shows the vertical reaction force curves in terms of the relative macroscopic compression displacement $\frac{\Delta}{H}$ given by the full and multi-scale models. Comparable results are observed. Figure 26a shows the deformed shape given by the full model and Fig. 26b shows the distribution of the Green–Lagrange strain obtained by the multi-scale simulation. It can be concluded that the second–order scheme provides an acceptable solution with a lower number of degrees of freedom.

For this problem the direct simulation requires a lot of resources (up to 30 GB memory) while the multi-scale computation is more efficient by the fact that a much smaller number of elements at the macro-scale problem are required and by the fact that the resolutions at the microscopic problems can be easily parallelized because they are totally independent.

6. Conclusions and perspectives

This work presents a general second–order multi–scale computational homogenization framework for cellular materials. Micro–buckling and macroscopic localization can occur and influence each other.

As the classical multi–scale computational homogenization schemes lose the solution uniqueness and face the strain localization problem when bucking occurs at the micro–scale, the second–order scheme incorporating the

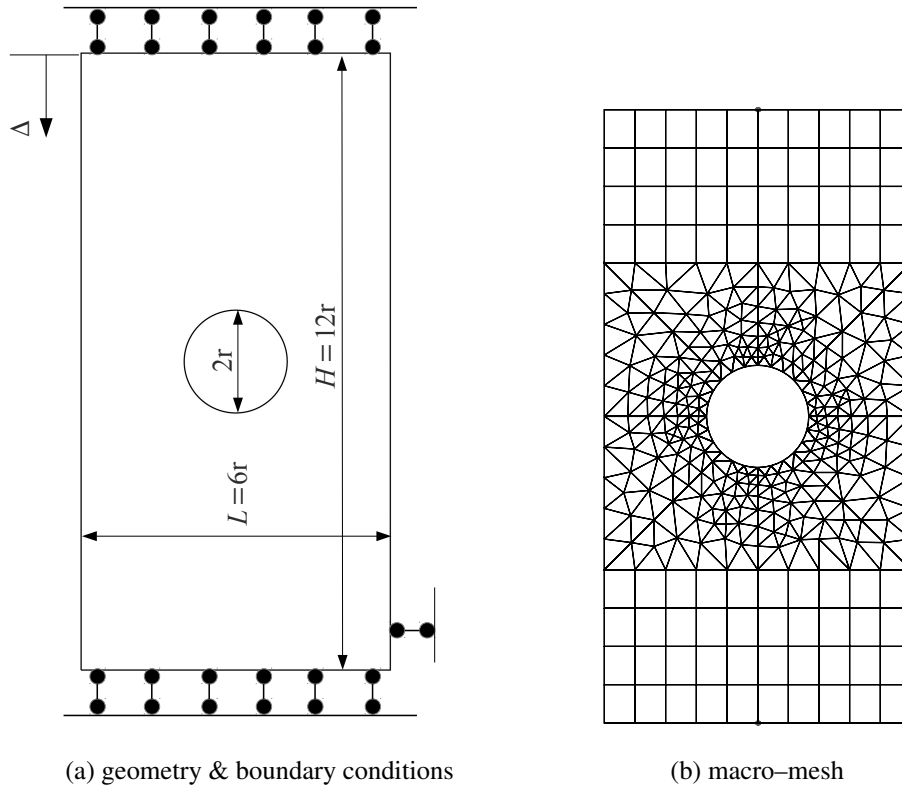(a) geometry & boundary conditions   (b) macro–mesh

Figure 24. Geometry and boundary condition used at the macro–scale (a) and the macro–mesh (b).

Mindlin strain gradient continuum is used at the macro–scale to capture the strain localization. The Mindlin contin-uum is solved using the discontinuous Galerkin method. At the micro–scale, as non–conformal meshes are generally obtained, the periodic boundary condition is enforced by using the polynomial interpolation method adapted for cells exhibiting important voids on the boundary. As the presences of instabilities are considered at both scales, the standard arc–length path following technique is adapted to a multi–scale computation.

This multi–scale model was used to study the uni–axial compression test of a specimen made of a hexagonal honeycomb with small imperfections. The micro–buckling has been considered and results were validated with direct numerical simulations of the structure demonstrating the ability of the method to capture the localization bands.

It was also found that on the one hand the size of the RVE for second–order scheme is bounded to avoid over-predictions and that on the other hand smaller RVE sizes are not always representative for structures with large imperfections, leading to softer predictions which are not physical. Thus this approach cannot be used for structures with high degrees of imperfection, but has been shown to predict with accuracy the behavior of structure made of regular micro–patterns for which a single repeated unit can be considered as a RVE. For higher imperfections, a sharper localization band can appear and only continuous–discontinuous multi–scale framework can be used.

Finally we have shown with the plate with a hole study that the method can be used to model larger problem made of cellular materials.

Appendix A. J2-hyperelastic–based elasto–plastic material model

Under large deformations the material model is based on the choice of a strain measure and on the definition of an elastic potential of the work-conjugate stress. The first Piola-Kirchhoff stress tensor **P** is considered and its work conjugate–strain measure is the deformation gradient **F**, with $J = \det(\mathbf{F}) > 0$ its Jacobian. For elasto–plastic materials,
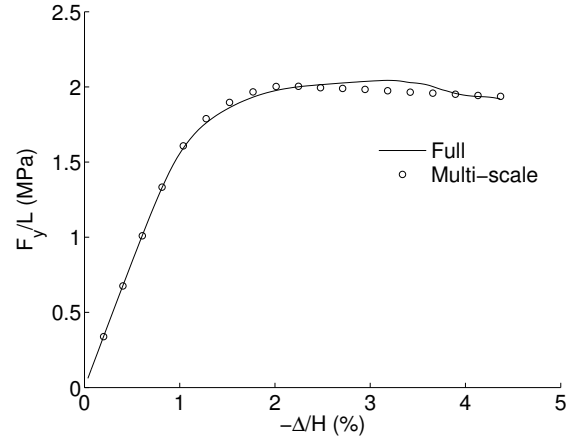
Figure 25. Reaction force *vs.* prescribed vertical displacement for the compression test of the rectangular plate with a central hole
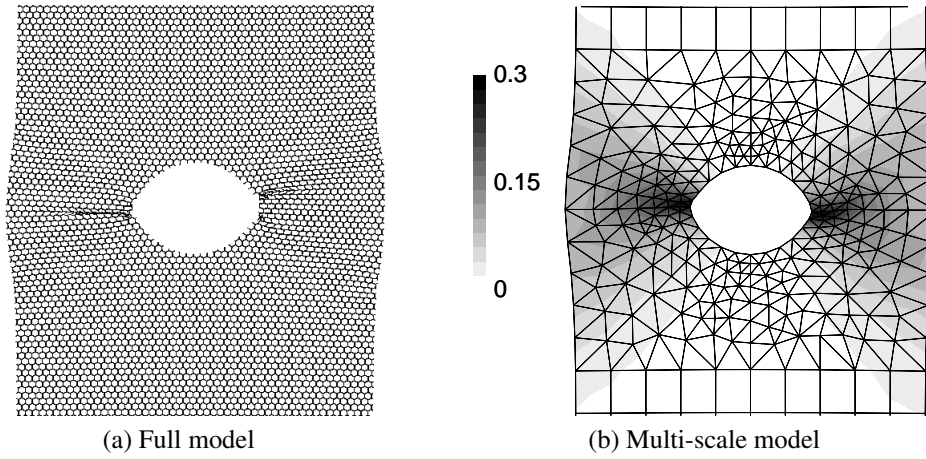

(a) Full model (b) Multi-scale model

Figure 26. Deformation shape obtained with the direct simulation (a) and distributions of the equivalent GreenLagrange strain obtained with the multi–scale simulation (b) at the final time.

a multiplicative decomposition of the deformation gradient is assumed

$$\mathbf{F} = \mathbf{F}^{\mathrm{e}}\mathbf{F}^{\mathrm{p}},\tag{A.1}$$

where $\mathbf{F}^{\mathrm{e}}$ and $\mathbf{F}^{\mathrm{p}}$ are the elastic and plastic parts of the deformation gradient, respectively. The material model is based on a hyperelastic formulation, with an elastic potential defined as

$$\Psi(\mathbf{C}^{\mathrm{e}}) = \frac{K}{2}\ln^2 J + \frac{G}{4}[\ln\mathbf{C}^{\mathrm{e}}]^{\mathrm{dev}} : [\ln\mathbf{C}^{\mathrm{e}}]^{\mathrm{dev}},\tag{A.2}$$

where $K = \frac{E}{3(1-2\nu)}$ and $G = \frac{E}{2(1+\nu)}$ are the bulk and shear moduli of the material, and where $[\ln\mathbf{C}^{\mathrm{e}}]^{\mathrm{dev}}$ is the deviatoric part of $\ln\mathbf{C}^{\mathrm{e}}$. Note that the defined elastic potential can only explicitly depends on the elastic deformation through the elastic right Cauchy strain tensor $\mathbf{C}^{\mathrm{e}} = \mathbf{F}^{\mathrm{e}\mathrm{T}}\mathbf{F}^{\mathrm{e}}$. Then, the first Piola-Kirchhoff stress tensor, given by $\mathbf{P} = 2\mathbf{F}\frac{\partial \Psi}{\partial \mathbf{C}}$, can

be derived as[1]

$$\begin{aligned} \mathbf{P} &= 2\mathbf{F}\left[\mathbf{F}^{\mathrm{p}-1}\frac{\partial\Psi(\mathbf{C}^{\mathrm{e}})}{\partial\mathbf{C}^{\mathrm{e}}}\mathbf{F}^{\mathrm{p}-\mathrm{T}}\right] \\ &= K\mathbf{F}^{\mathrm{-T}}\ln J + \mathbf{F}^{\mathrm{e}}\left[2G\mathbf{C}^{\mathrm{e}-1}\cdot(\ln\sqrt{\mathbf{C}^{\mathrm{e}}})^{\mathrm{dev}}\right]\mathbf{F}^{\mathrm{p}\text{-}\mathrm{T}}. \end{aligned} \tag{A.3}$$

In order to obtain the elastic and plastic parts of the deformation gradient in Equation (A.1), the J_2-flow theory, expressed in terms of the Kirchhoff stress, is used in this work. To this end, the Kirchhoff stress $\boldsymbol{\tau} = \mathbf{PF}^{\mathrm{T}}$ needs to be calculated, via

$$\boldsymbol{\tau} = p'\mathbf{I} + \mathbf{F}^{\mathrm{e}}\left[2G\mathbf{C}^{\mathrm{e}-1}\cdot(\ln\sqrt{\mathbf{C}^{\mathrm{e}}})^{\mathrm{dev}}\right]\mathbf{F}^{\mathrm{e}\mathrm{T}}, \tag{A.4}$$

where $p' = (K\ln J)$ is the pressure, and where the second term on the right hand side of Equation (A.4) is the deviatoric part of the Kirchhoff stress, $\boldsymbol{\tau}^{\mathrm{dev}}$, which yields the equivalent von Mises stress $\tau^{\mathrm{eq}} = \sqrt{\frac{3}{2}\boldsymbol{\tau}^{\mathrm{dev}}:\boldsymbol{\tau}^{\mathrm{dev}}}$. According to the J_2–elasto–plasticity theory, the von Mises stress criterion reads

$$f = \tau^{\mathrm{eq}} - R(p) - \sigma_y^0 \leqslant 0, \tag{A.5}$$

where f is the yield surface, σ_y^0 is the initial yield stress, $R(p) \geqslant 0$ is the isotropic hardening stress, and where p is an internal variable characterizing the irreversible behavior, as the equivalent plastic strain in small deformation. Equation (A.5) is completed by the normal plastic flow, which gives the increment of the plastic deformation gradient during the time step between the configurations "n" and "$n + 1$", and reads

$$\begin{cases} \mathbf{F}^{\mathrm{p}}{}_{n+1} = \exp(\triangle p\mathbf{N}^{\mathrm{p}})\cdot\mathbf{F}^{\mathrm{p}}{}_n, \\ \mathbf{N}^{\mathrm{p}} = \frac{\partial f}{\partial\boldsymbol{\sigma}} = \frac{3}{2}\frac{\boldsymbol{\tau}^{\mathrm{dev}}}{\tau^{\mathrm{eq}}}. \end{cases} \tag{A.6}$$

Practically, the normal of the yield surface $\mathbf{N}^{\mathrm{p}}$ is calculated from the elastic predictor. By derivation of this material model, one can also compute

$$\mathbf{L} = \frac{\partial\mathbf{P}}{\partial\mathbf{F}}, \quad\text{and} \tag{A.7}$$

$$\mathbb{F}^{\mathrm{p}} = \frac{\partial\mathbf{F}^{\mathrm{p}}}{\partial\mathbf{F}}. \tag{A.8}$$

These close form expressions and more details can be found in the framework proposed by [54].

The resolution of the system of Eqs. (A.1-A.6) follows the predictor-corrector scheme during the time interval $[t_n\ t_{n+1}]$ described by [54], and which can be summarized as follows

1. Predictor step. The plastic deformation gradient tensor is initialized to the value at the previous step $\mathbf{F}^{\mathrm{ppr}} = \mathbf{F}_n^{\mathrm{p}}$ leading to the right Cauchy elastic predictor $\mathbf{C}^{\mathrm{epr}} = \mathbf{F}^{\mathrm{ppr}-T}\mathbf{F}_{n+1}^T\mathbf{F}_{n+1}\mathbf{F}^{\mathrm{ppr}-1}$. As the plastic flow is independent from the rotation tensor, the plastic correction can be computed in an unrotated configuration and, using Eq. (A.4), the elastic predictor reads

$$(\tau^{\mathrm{pr}})^{\mathrm{dev}} = 2G\left(\ln\sqrt{\mathbf{C}^{\mathrm{epr}}}\right)^{\mathrm{dev}}, \tag{A.9}$$

and the plastic flow direction (A.6) is readily deduced as being

$$\mathbf{N}^{\mathrm{p}} = \sqrt{\frac{3}{2}}\frac{\left(\ln\sqrt{\mathbf{C}^{\mathrm{epr}}}\right)^{\mathrm{dev}}}{\sqrt{\left(\ln\sqrt{\mathbf{C}^{\mathrm{epr}}}\right)^{\mathrm{dev}}:\left(\ln\sqrt{\mathbf{C}^{\mathrm{epr}}}\right)^{\mathrm{dev}}}}. \tag{A.10}$$

---

[1]Using $\frac{\partial\ln\mathbf{C}^{\mathrm{e}}:\ln\mathbf{C}^{\mathrm{e}}}{\partial\mathbf{C}^{\mathrm{e}}} = 2\mathbf{C}^{\mathrm{e}-1}\cdot\ln\mathbf{C}^{\mathrm{e}} = 2\ln\mathbf{C}^{\mathrm{e}}\cdot\mathbf{C}^{\mathrm{e}-1} = 2\mathbf{U}^{\mathrm{e}-1}\cdot\ln\mathbf{C}^{\mathrm{e}}\cdot\mathbf{U}^{\mathrm{e}-1}$, where $\mathbf{U}^{\mathrm{e}}$ is the symmetric part of $\mathbf{F}^{\mathrm{e}}$ and $\mathrm{tr}\left(\ln\left(\sqrt{\mathbf{C}^{\mathrm{e}}}\right)\right) = \ln(J)$.

2. Correction step. If the von Mises criterion (A.5) is not satisfied using this predictor, *i.e.* $f = \left((\tau^{\mathrm{pr}})^{\mathrm{dev}}\right)^{\mathrm{eq}} - R(p_n) - \sigma_{\mathrm{Y}} > 0$, one iteratively computes the accumulated plastic strain increment Δp such that the corrotational Kirchhoff tensor satisfies the von Mises criterion:

$$\mathbf{F}^{\mathrm{e}} = \mathbf{F}\,(\mathbf{F}^{\mathrm{ppr}})^{-1} \cdot (\exp(\triangle p \mathbf{N}^{\mathrm{p}}))^{-1} \tag{A.11}$$

$$\left(\ln \sqrt{\mathbf{C}^{\mathrm{e}}}\right)^{\mathrm{dev}} = \left(\ln \sqrt{\mathbf{C}^{\mathrm{epr}}}\right)^{\mathrm{dev}} - \Delta p \mathbf{N}^{\mathrm{p}}\,, \tag{A.12}$$

$$(\tau^{\mathrm{cor}})^{\mathrm{dev}} = 2G \left(\ln \sqrt{\mathbf{C}^{\mathrm{e}}}\right)^{\mathrm{dev}}\,, \tag{A.13}$$

$$f = \left((\tau^{\mathrm{cor}})^{\mathrm{dev}}\right)^{\mathrm{eq}} - R(p_n + \Delta p) - \sigma_{\mathrm{Y}} = 0\,. \tag{A.14}$$

Note that Eq. (A.12) results from Eq. (A.6), from Eq. (A.11), and from the following properties

$$\mathbf{C}^{\mathrm{e}} = (\exp(\triangle p \mathbf{N}^{\mathrm{p}}))^{-T} \cdot \mathbf{C}^{\mathrm{epr}} \cdot (\exp(\triangle p \mathbf{N}^{\mathrm{p}}))^{-1}\,,$$

$$\log\left((\mathbf{C}^{\mathrm{e}})^{\mathrm{dev}}\right) = \log\left((\mathbf{C}^{\mathrm{epr}})^{\mathrm{dev}}\right) - 2\Delta p \mathbf{N}^{\mathrm{p}}\,, \tag{A.15}$$

where we have used the permutativity properties of $\mathbf{N}^{\mathrm{p}}$ and $(\mathbf{C}^{\mathrm{epr}})^{\mathrm{dev}}$.

3. Final state. The elastic and plastic deformation gradient are respectively obtained from Eqs. (A.11) and (A.6), and the effective Piola-Kirchhoff stress tensor from Eq. (A.3).

Appendix B. Parallel implementation

In this section, the finite element implementation of the path–following method in the context of the DG–based second–order computational homogenization is presented.
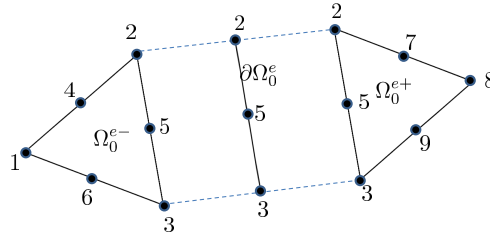

Figure B.27. Interface element $\partial \Omega_0^e$ between two adjacent quadratic triangles Ω_0^{e+} and Ω_0^{e-}.

At the macroscopic scale, for the Mindlin strain gradient problem, the interpolation polynomial order is at least of the second order. Thus at least quadratic elements are used with a usual Gauss under–integration. At each element boundary, an interface element is inserted, see Fig. B.27, and is defined from the degrees of freedom of two adjacent elements Ω_0^{e+} and Ω_0^{e-}. The Gauss points of this interface element are duplicated with a positive and a negative Gauss points at each position so that they respectively belong to the positive and negative elements in order to evaluate the jump and mean values of the interface terms (16, 17). At each Gauss point of both the bulk and interface elements, a separate microscopic BVP is attached. Because of the introduction of some randomness in the micro–structure, each macroscopic material point is associated with a local RVE which differs from the other RVEs attached to the other macroscopic positions. In order to take into account this randomness, a library of RVE meshes with a certain number of examples is generated. Each microscopic BVP located at a macroscopic position takes a random RVE mesh from the mesh library. However at each Gauss point of an interface element, the positive and negative Gauss points located at the same position take the same RVE geometry.

The computation is performed in parallel. At the macroscopic scale, the mesh is partitioned on several processors, see Fig. B.28. The macroscopic problem is thus solved by using face–based ghost elements. The ghost elements allows to compute the interface terms at the boundaries of each processor and thus to ensure the compatibility between the partitions. This efficient methodology is possible because of the discontinuous Galerkin framework, see [37, 38] for details. At the microscopic scale, each microscopic BVP is solved in serial, but as a large number of microscopic
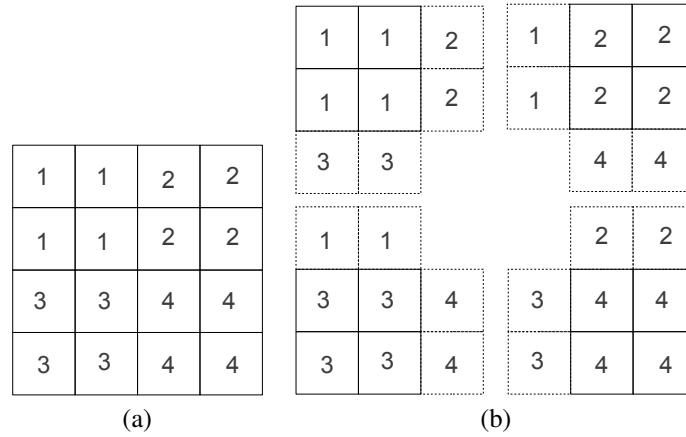
Figure B.28. Parallelization of the macroscopic problem: (a) initial mesh with the partition numbers and (b) partitioned mesh with the associated ghost elements plotted in dotted line.

BVPs are considered for each macro–scale processor, the microscopic BVPs of a macro–scale partition are distributed to different processors, see Fig. B.29. This parallelization on a double level is summarized as follows. The macroscopic BVP is distributed on n "macro–processors". For each "macro–processor", the underlying microscopic BVPs are distributed on p "micro–processors". Each "micro–processor" contains j microscopic BVPs. With this strategy, any number of processors can be used, see Fig. B.29.

The "initialization block" of the multi–scale scheme in Fig. 5 thus contains the following steps:

1. Initialize the macroscopic BVP:
   - Load the macroscopic mesh.
   - Distribute the macroscopic BVP to the macro–processors, see Fig. B.29.
   - Create all the macroscopic Gauss points.

2. Load the RVE meshes from the micro–mesh library:
   - Attach a microscopic BVP at each macroscopic Gauss point. Each microscopic BVP located on a macroscopic position takes a random RVE mesh from the micro–mesh library.
   - However at each Gauss point of an interface element, the positive and negative Gauss points located at the same position take the same RVE geometry.

3. Distribute the microscopic BVPs belonging to one "macro–processor" to several "micro–processors", see Fig. B.29.

4. Initiate every microscopic BVP as follows:
   - Assign the material laws to the microscopic constituents.
   - Compute the constraint matrix $\mathbf{C}$ in (46) and the projection matrices $\mathbf{R}$ and $\mathbf{Q}$.
   - Compute the initial tangent operators $\bar{\mathbf{L}}^0, \bar{\mathbf{L}}_J^0, \bar{\mathbf{J}}_L^0$ and $\bar{\mathbf{J}}^0$ required for the interface terms of the DG formulation, see [27] for details.
   - Send the values of these elastic tangent operators to the macroscopic BVP.

5. Compute the macroscopic load vector following Eq. (22).

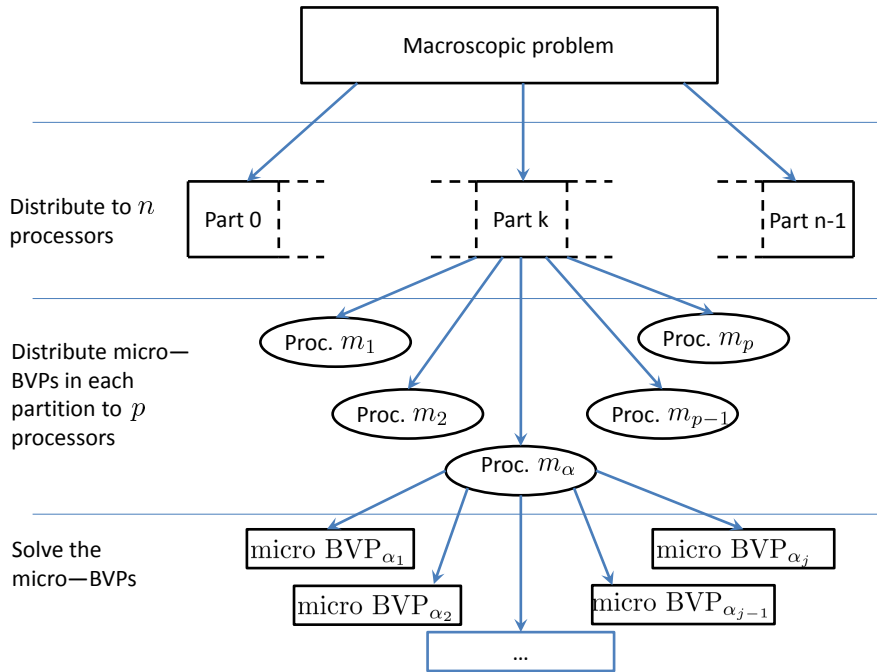This framework has been implemented in the parallel code Gmsh [55].

Figure B.29. Parallel multi–scale computation. The macroscopic problem is parallelized on *n* "macro–processors" and solved using face–based ghost elements. The microscopic BVPs at each macro–processor are distributed on *p* "micro–processors" and naturally distinct problems. Each "micro–processor" contains *j* micro BVPs.

Appendix C. Random perturbation of an hexagonal honeycomb

We use the Voronoï tessellation technique to generate the regular and perturbed hexagons. From the regular set of points which generate the regular hexagons with edge length *l*, the perturbed set of points are created by modifying the point coordinates, see Fig. Appendix C, such that

$$x_i = x_i + \delta d \cos(\phi) \text{ and}$$
$$y_i = y_i + \delta d \sin(\phi), \tag{C.1}$$

where *d* is a random value in [0 *l*], where ϕ is a random value in [0 2π] and where δ is the control parameter which allows controlling the perturbation level of the micro–structure. The same thickness *t* is used for all the cell walls in order to generate the complete structure.
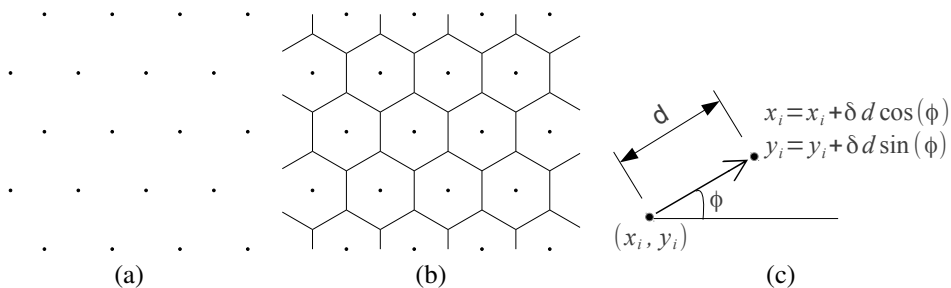

(a) (b) (c)

Figure C.30. Voronoï diagram of the hexagonal honeycomb: (a) regular control points, (b) generated regular hexagons and (c) coordinate perturbation at each control point *i*. The coordinate perturbation is controlled by ϕ, which is a random angle in [0 2π], by *d* which is the random distance in [0 *l*] where *l* is edge length of regular hexagon and by δ which is the control parameter defining the perturbation intensity.

References

[1] M. F. A. Lorna J. Gibson, Cellular solids: structure and properties (2nd ed), Cambridge University Press, 1997.

[2] E. Andrews, G. Gioux, P. Onck, L. Gibson, Size effects in ductile cellular solids. part ii: experimental results, International Journal of Mechanical Sciences 43 (3) (2001) 701 – 713. doi:10.1016/S0020-7403(00)00043-6.
URL http://www.sciencedirect.com/science/article/pii/S0020740300000436

[3] S. Papka, S. Kyriakides, Experiments and full-scale numerical simulations of in-plane crushing of a honeycomb, Acta Materialia 46 (8) (1998) 2765 – 2776. doi:10.1016/S1359-6454(97)00453-9.
URL http://www.sciencedirect.com/science/article/pii/S1359645497004539

[4] H. Zhu, N. Mills, The in-plane non-linear compression of regular honeycombs, International Journal of Solids and Structures 37 (13) (2000) 1931 – 1949. doi:http://dx.doi.org/10.1016/S0020-7683(98)00324-2.
URL http://www.sciencedirect.com/science/article/pii/S0020768398003242

[5] H. Bart-Smith, A.-F. Bastawros, D. Mumm, A. Evans, D. Sypeck, H. Wadley, Compressive deformation and yielding mechanisms in cellular al alloys determined using x-ray tomography and surface strain mapping, Acta Materialia 46 (10) (1998) 3583 – 3592. doi:http://dx.doi.org/10.1016/S1359-6454(98)00025-1.
URL http://www.sciencedirect.com/science/article/pii/S1359645498000251

[6] W.-Y. Jang, S. Kyriakides, On the crushing of aluminum open-cell foams: Part i. experiments, International Journal of Solids and Structures 46 (34) (2009) 617 – 634. doi:http://dx.doi.org/10.1016/j.ijsolstr.2008.09.008.
URL http://www.sciencedirect.com/science/article/pii/S0020768308003788

[7] C. Tekoglu, L. Gibson, T. Pardoen, P. Onck, Size effects in foams: Experiments and modeling, Progress in Materials Science 56 (2) (2011) 109 – 138. doi:10.1016/j.pmatsci.2010.06.001.
URL http://www.sciencedirect.com/science/article/pii/S0079642510000393

[8] K. Mangipudi, P. Onck, Multiscale modelling of damage and failure in two-dimensional metallic foams, Journal of the Mechanics and Physics of Solids In Press, Accepted Manuscript (2011) –. doi:DOI: 10.1016/j.jmps.2011.02.008.
URL http://www.sciencedirect.com/science/article/B6TXB-52CYKTW-1/2/26d568f7ec550970f7f16743634351ef

[9] C. Chen, N. Fleck, Size effects in the constrained deformation of metallic foams, Journal of the Mechanics and Physics of Solids 50 (5) (2002) 955 – 977. doi:http://dx.doi.org/10.1016/S0022-5096(01)00128-4.
URL http://www.sciencedirect.com/science/article/pii/S0022509601001284

[10] S. Forest, J.-S. Blazy, Y. Chastel, F. Moussy, Continuum modeling of strain localization phenomena in metallic foams, Journal of Materials Science 40 (2005) 5903–5910, 10.1007/s10853-005-5041-6.
URL http://dx.doi.org/10.1007/s10853-005-5041-6

[11] A. Hanssen, O. Hopperstad, M. Langseth, H. Ilstad, Validation of constitutive models applicable to aluminium foams, International Journal of Mechanical Sciences 44 (2) (2002) 359 – 406. doi:http://dx.doi.org/10.1016/S0020-7403(01)00091-1.
URL http://www.sciencedirect.com/science/article/pii/S0020740301000911

[12] H. Sehlhorst, R. Jnicke, A. Dster, E. Rank, H. Steeb, S. Diebels, Numerical investigations of foam-like materials by nested high-order finite element methods, Computational Mechanics 45 (2009) 45–59, 10.1007/s00466-009-0414-3.
URL http://dx.doi.org/10.1007/s00466-009-0414-3

[13] V. G. Kouznetsova, Computational homogenization for the multi-scale analysis of multi-phase materials, Ph.D. thesis, Technische Universiteit Eindhoven (2002).

[14] V. G. Kouznetsova, M. G. D. Geers, W. A. M. Brekelmans, Multi-scale second-order computational homogenization of multi-phase materials: a nested finite element solution strategy, Computer Methods in Applied Mechanics and Engineering 193 (48-51) (2004) 5525–5550, advances in Computational Plasticity. doi:DOI: 10.1016/j.cma.2003.12.073.
URL http://www.sciencedirect.com/science/article/B6V29-4D4D4JV-3/2/6fd8ac06299b9a26d8a17438871de868

[15] T. Ebinger, H. Steeb, S. Diebels, Modeling macroscopic extended continua with the aid of numerical homogenization schemes, Computational Materials Science 32 (34) (2005) 337 – 347. doi:http://dx.doi.org/10.1016/j.commatsci.2004.09.034.
URL http://www.sciencedirect.com/science/article/pii/S0927025604002125

[16] P. R., Onck, Cosserat modeling of cellular solids, Comptes Rendus Mcanique 330 (11) (2002) 717 – 722. doi:10.1016/S1631-0721(02)01529-2.
URL http://www.sciencedirect.com/science/article/pii/S1631072102015292

[17] J. Yvonnet, H. Zahrouni, M. Potier-Ferry, A model reduction method for the post-buckling analysis of cellular microstructures, Computer Methods in Applied Mechanics and Engineering 197 (1-4) (2007) 265 – 280. doi:DOI: 10.1016/j.cma.2007.07.026.
URL http://www.sciencedirect.com/science/article/pii/S0045782507003271

[18] M. Laroussi, K. Sab, A. Alaoui, Foam mechanics: nonlinear response of an elastic 3d-periodic microstructure, International Journal of Solids and Structures 39 (13-14) (2002) 3599 – 3623. doi:DOI: 10.1016/S0020-7683(02)00172-5.
URL http://www.sciencedirect.com/science/article/pii/S0020768302001725

[19] N. Ohno, D. Okumura, H. Noguchi, Microscopic symmetric bifurcation condition of cellular solids based on a homogenization theory of finite deformation, Journal of the Mechanics and Physics of Solids 50 (5) (2002) 1125 – 1153. doi:DOI: 10.1016/S0022-5096(01)00106-5.
URL http://www.sciencedirect.com/science/article/pii/S0022509601001065

[20] D. Okumura, N. Ohno, H. Noguchi, Elastoplastic microscopic bifurcation and post-bifurcation behavior of periodic cellular solids, Journal of the Mechanics and Physics of Solids 52 (3) (2004) 641 – 666. doi:10.1016/j.jmps.2003.07.002.
URL http://www.sciencedirect.com/science/article/pii/S0022509603001248

[21] D. Okumura, N. Ohno, H. Noguchi, Post-buckling analysis of elastic honeycombs subject to in-plane biaxial compression, International Journal of Solids and Structures 39 (13-14) (2002) 3487 – 3503. doi:10.1016/S0020-7683(02)00165-8.
URL http://www.sciencedirect.com/science/article/pii/S0020768302001658

[22] M. G. D. Geers, V. G. Kouznetsova, W. A. M. Brekelmans, Multi-scale computational homogenization: Trends and challenges, Journal of

Computational and Applied Mathematics 234 (7) (2010) 2175–2182, fourth International Conference on Advanced COmputational Methods in ENgineering (ACOMEN 2008). doi:DOI: 10.1016/j.cam.2009.08.077.
URL `http://www.sciencedirect.com/science/article/B6TYH-4X1J73B-8/2/ee8d9b69133503eaf14b00ddbe1bd8f5`

[23] V. P. Nguyen, O. Lloberas-Valls, M. Stroeven, L. J. Sluys, Computational homogenization for multiscale crack modeling. implementational and computational aspects, International Journal for Numerical Methods in Engineering (2011) n/a–n/adoi:10.1002/nme.3237.
URL `http://dx.doi.org/10.1002/nme.3237`

[24] T. Massart, R. Peerlings, M. Geers, An enhanced multi-scale approach for masonry wall computations, International Journal for Numerical Method Engineering 69 (5) (2007) 1022–1059.

[25] E. Coenen, V. Kouznetsova, M. Geers, Multi-scale continuousdiscontinuous framework for computational-homogenizationlocalization, Journal of the Mechanics and Physics of Solids 60 (8) (2012) 1486 – 1507. doi:http://dx.doi.org/10.1016/j.jmps.2012.04.002.
URL `http://www.sciencedirect.com/science/article/pii/S0022509612000749`

[26] L. Kaczmarczyk, C. J. Pearce, N. Bićanić, Scale transition and enforcement of rve boundary conditions in second-order computational homogenization, Int. J. Numer. Meth. Engng. 74 (3) (2008) 506–522.
URL `http://dx.doi.org/10.1002/nme.2188`

[27] V.-D. Nguyen, G. Becker, L. Noels, Multiscale computational homogenization methods with a gradient enhanced scheme based on the discontinuous galerkin formulation, Computer Methods in Applied Mechanics and Engineering 260 (0) (2013) 63 – 77. doi:http://dx.doi.org/10.1016/j.cma.2013.03.024.
URL `http://www.sciencedirect.com/science/article/pii/S0045782513000832`

[28] G. A. Wempner, Discrete approximations related to nonlinear theories of solids, International Journal of Solids and Structures 7 (11) (1971) 1581 – 1599. doi:http://dx.doi.org/10.1016/0020-7683(71)90038-2.
URL `http://www.sciencedirect.com/science/article/pii/0020768371900382`

[29] E. Riks, An incremental approach to the solution of snapping and buckling problems, International Journal of Solids and Structures 15 (7) (1979) 529 – 551. doi:http://dx.doi.org/10.1016/0020-7683(79)90081-7.
URL `http://www.sciencedirect.com/science/article/pii/0020768379900817`

[30] P. Bellini, A. Chulya, An improved automatic incremental algorithm for the efficient solution of nonlinear finite element equations, Computers & Structures 26 (1¢2) (1987) 99 – 110. doi:http://dx.doi.org/10.1016/0045-7949(87)90240-9.
URL `http://www.sciencedirect.com/science/article/pii/0045794987902409`

[31] E. Riks, On formulations of path-following techniques for structural stability analysis, NASA STI/Recon Technical Report N 931 (1992) 16346–+.

[32] M. Fafard, B. Massicotte, Geometrical interpretation of the arc-length method, Computers & Structures 46 (4) (1993) 603 – 615. doi:http://dx.doi.org/10.1016/0045-7949(93)90389-U.
URL `http://www.sciencedirect.com/science/article/pii/004579499390389U`

[33] Z. Zhou, D. Murray, An incremental solution technique for unstable equilibrium paths of shell structures, Computers & Structures 55 (5) (1995) 749 – 759. doi:10.1016/0045-7949(94)00474-H.
URL `http://www.sciencedirect.com/science/article/pii/004579499400474H`

[34] R. Kouhia, M. Mikkola, Some aspects on efficient path-following, Computers & Structures 72 (45) (1999) 509 – 524. doi:http://dx.doi.org/10.1016/S0045-7949(98)00336-8.
URL `http://www.sciencedirect.com/science/article/pii/S0045794998003368`

[35] P. L. Grognec, A. L. van, Elastoplastic bifurcation and collapse of axially loaded cylindrical shells, International Journal of Solids and Structures 45 (1) (2008) 64 – 86. doi:http://dx.doi.org/10.1016/j.ijsolstr.2007.07.017.
URL `http://www.sciencedirect.com/science/article/pii/S0020768307002934`

[36] P. L. Grognec, P. Casari, D. Choqueuse, Influence of residual stresses and geometric imperfections on the elastoplastic collapse of cylindrical tubes under external pressure, Marine Structures 22 (4) (2009) 836 – 854. doi:http://dx.doi.org/10.1016/j.marstruc.2009.09.003.
URL `http://www.sciencedirect.com/science/article/pii/S0951833909000525`

[37] G. Becker, C. Geuzaine, L. Noels, A one field full discontinuous galerkin method for kirchhofflove shells applied to fracture mechanics, Computer Methods in Applied Mechanics and Engineering 200 (4546) (2011) 3223 – 3241. doi:10.1016/j.cma.2011.07.008.
URL `http://www.sciencedirect.com/science/article/pii/S0045782511002490`

[38] L. Wu, D. Tjahjanto, G. Becker, A. Makradi, A. Jrusalem, L. Noels, A micromeso-model of intra-laminar fracture in fiber-reinforced composites based on a discontinuous galerkin/cohesive zone method, Engineering Fracture Mechanics 104 (0) (2013) 162 – 183. doi:http://dx.doi.org/10.1016/j.engfracmech.2013.03.018.
URL `http://www.sciencedirect.com/science/article/pii/S0013794413001252`

[39] T. Kanit, S. Forest, I. Galliet, V. Mounoury, D. Jeulin, Determination of the size of the representative volume element for random composites: statistical and numerical approach, International Journal of Solids and Structures 40 (13-14) (2003) 3647–3679. doi:DOI: 10.1016/S0020-7683(03)00143-4.
URL `http://www.sciencedirect.com/science/article/B6VJS-48GDV9K-1/2/2dd6cda9c49706ed2c969bdea531bb50`

[40] K. Terada, M. Hori, T. Kyoya, N. Kikuchi, Simulation of the multi-scale convergence in computational homogenization approaches, International Journal of Solids and Structures 37 (16) (2000) 2285–2311. doi:DOI: 10.1016/S0020-7683(98)00341-2.
URL `http://www.sciencedirect.com/science/article/B6VJS-3YDFYCH-4/2/788d085d620c6c5ae804d8c4e4f8ae9b`

[41] F. Larsson, K. Runesson, S. Saroukhani, R. Vafadari, Computational homogenization based on a weak format of micro-periodicity for rve-problems, Computer Methods in Applied Mechanics and Engineering 200 (1-4) (2011) 11–26. doi:DOI: 10.1016/j.cma.2010.06.023.
URL `http://www.sciencedirect.com/science/article/B6V29-50J9GSY-1/2/50ad840717a7cc397ab171da344df990`

[42] V.-D. Nguyen, E. Bchet, C. Geuzaine, L. Noels, Imposing periodic boundary condition on arbitrary meshes by polynomial interpolation, Computational Materials Science 55 (0) (2012) 390 – 406. doi:10.1016/j.commatsci.2011.10.017.
URL `http://www.sciencedirect.com/science/article/pii/S0927025611005866`

[43] E. Coenen, V. Kouznetsova, M. Geers, Novel boundary conditions for strain localization analyses in microstructural volume elements, Inter-

national Journal for Numerical Methods in Engineering 90 (1) (2012) 1–21. doi:10.1002/nme.3298.
URL `http://dx.doi.org/10.1002/nme.3298`

[44] Z. Yuan, J. Fish, Toward realization of computational homogenization in practice, Int. J. Numer. Meth. Engng. 73 (3) (2008) 361–380.
URL `http://dx.doi.org/10.1002/nme.2074`

[45] J. M. Tyrus, M. Gosz, E. DeSantiago, A local finite element implementation for imposing periodic boundary conditions on composite micromechanical models, International Journal of Solids and Structures 44 (9) (2007) 2972–2989. doi:DOI: 10.1016/j.ijsolstr.2006.08.040.
URL `http://www.sciencedirect.com/science/article/B6VJS-4KW5FH7-2/2/5ff1cecbcb5cdcf33cab7c7f6f6a1935`

[46] R. Mindlin, Second gradient of strain and surface-tension in linear elasticity, International Journal of Solids and Structures 1 (1965) 417–438. doi:No doi.
URL `http://isn-csm.mit.edu/literature/1965-IJSS-Mindlin.pdf`

[47] C. Miehe, A. Koch, Computational micro-to-macro transitions of discretized microstructures undergoing small strains, Archive of Applied Mechanics 72 (4) (2002) 300–317, 10.1007/s00419-002-0212-2.
URL `http://dx.doi.org/10.1007/s00419-002-0212-2`

[48] Mark, Ainsworth, Essential boundary conditions and multi-point constraints in finite element analysis, Computer Methods in Applied Mechanics and Engineering 190 (48) (2001) 6323 – 6339. doi:10.1016/S0045-7825(01)00236-5.
URL `http://www.sciencedirect.com/science/article/pii/S0045782501002365`

[49] V. Kouznetsova, M. Geers, W. Brekelmans, Size of a representative volume element in a second-order computational homogenization framework, Int. Jnl. Multiscale Comp. Eng. 2 (4) (2004) 575–598.

[50] R. Peerlings, L. Poh, M. Geers, An implicit gradient plasticitydamage theory for predicting size effects in hardening and softening, Engineering Fracture Mechanics 95 (0) (2012) 2 – 12, ¡ce:title¿Cracks in Microstructures and Engineering Components¡/ce:title¿. doi:http://dx.doi.org/10.1016/j.engfracmech.2011.12.016.
URL `http://www.sciencedirect.com/science/article/pii/S0013794412000999`

[51] C. Tekoglu, P. R. Onck, Size effects in two-dimensional voronoi foams: A comparison between generalized continua and discrete models, Journal of the Mechanics and Physics of Solids 56 (12) (2008) 3541 – 3564. doi:10.1016/j.jmps.2008.06.007.
URL `http://www.sciencedirect.com/science/article/pii/S0022509608001142`

[52] D. Lam, F. Yang, A. Chong, J. Wang, P. Tong, Experiments and theory in strain gradient elasticity, Journal of the Mechanics and Physics of Solids 51 (8) (2003) 1477 – 1508. doi:http://dx.doi.org/10.1016/S0022-5096(03)00053-X.
URL `http://www.sciencedirect.com/science/article/pii/S002250960300053X`

[53] N. Fleck, J. Hutchinson, Strain gradient plasticity, Vol. 33 of Advances in Applied Mechanics, Elsevier, 1997, pp. 295 – 361. doi:http://dx.doi.org/10.1016/S0065-2156(08)70388-0.
URL `http://www.sciencedirect.com/science/article/pii/S0065215608703880`

[54] A. Cuitiño, M. Ortiz, A material-independent method for extending stress update algorithms from small-strain plasticity to finite plasticity with multiplicative kinematics, Engineering Computations 9 (1992) 437–451. doi:10.1108/eb023876.
URL `http://dx.doi.org/10.1108/eb023876`

[55] C. Geuzaine, J.-F. Remacle, Gmsh: A 3-d finite element mesh generator with built-in pre- and post-processing facilities, International Journal for Numerical Methods in Engineering 79 (11) (2009) 1309–1331.
URL `http://dx.doi.org/10.1002/nme.2579`